High Amplitude Redox Changes in the late Early Triassic of South China and the Smithian/Spathian extinction

Y.D. Sun[1, 2,*], P.B. Wignall[3], M.M. Joachimski[2], D.P.G. Bond[4], S.E. Grasby[5, 6], S. Sun[7], C.B. Yan[8], L.N. Wang[1], Y.L. Chen[9], X.L. Lai[1]

Please cite the full version of this article as:

Y.D. Sun, P.B. Wignall, M.M. Joachimski, D.P.G. Bond, S.E. Grasby, S. Sun, C.B. Yan, L.N. Wang, Y.L. Chen, X.L. Lai, High amplitude redox changes in the late Early Triassic of South China and the Smithian–Spathian extinction, Palaeogeography, Palaeoclimatology, Palaeoecology, Volume 427, 1 June 2015, Pages 62-78, ISSN 0031-0182, http://dx.doi.org/10.1016/j.palaeo.2015.03.038.

High Amplitude Redox Changes in the late Early Triassic of South China and the Smithian/Spathian extinction

Y.D. Sun[1,2,*], P.B. Wignall[3], M.M. Joachimski[2], D.P.G. Bond[4], S.E. Grasby[5,6], S. Sun[7], C.B. Yan[8], L.N. Wang[1], Y.L. Chen[9], X.L. Lai[1]

1. State Key Laboratory of Biogeology and Environmental Geology, China University of Geosciences (Wuhan), Wuhan 430074, P.R. China

2. GeoZentrum Nordbayern, Universität Erlangen-Nürnberg, Schlossgarten 5, 91054 Erlangen, Germany

3. School of Earth and Environment, University of Leeds, Leeds LS2 9JT, UK

4. Department of Geography, Environment and Earth Sciences, University of Hull, Hull, HU6 7RX, United Kingdom

5. Geological Survey of Canada, 3303 33rd Street N.W., Calgary, Alberta, T2L 2A7, Canada

6. Department of Geoscience, University of Calgary, 2500 University Dr. N.W., Calgary Alberta, T2N 1N4, Canada

7. Department of Earth Sciences, University of Hong Kong, Pokfulam Road, Hong Kong

8. Wuhan Center of Geological Survey, Guanggu Road 69, Wuhan 430074, P.R. China

9. Institute of Earth Sciences, University of Graz, Heinrichstrasse 26, 8010 Graz, Austria

*corresponding author: E-mail: yadong.sun@cug.edu.cn (Y.D. Sun)

Abstract

The Early Triassic was a time of remarkably high temperatures, large carbon cycle perturbations and episodes of widespread ocean anoxia. The sediments in the Nanpanjiang Basin of South China provide superb opportunities to examine the sedimentary response to these extreme conditions especially during the crisis interval at the Smithian-Spathian (S-S) boundary. We have investigated a deep water section at Jiarong and a shallower water section at Mingtang. These contain a range of facies including black shales, micritic limestone units and rudaceous carbonate event beds that include flat pebble conglomerates and breccia debrites that bear similarities to the hybrid event beds seen in clastic turbidite successions.

Redox proxies (pyrite framboids and trace metals) reveal that widespread anoxia in the late Smithian persisted into the *Novispathodus pingdingshanensis* Zone of the early Spathian before a sharp transition to highly oxygenated “griotte facies” (red marine strata) in the *Icriospathodus collinsoni* Zone that records an “oxic rebound”. Benthic faunas are locally common but of low diversity and dominated by thin-shelled bivalves and ostracodes with small foraminifers and exceptionally rare fish remains. Bioturbation was intense only in the early-middle Spathian (*Ic. collinsoni* conodont zone) Griotte facies. Anoxia and extremely high temperatures probably played a role in severely restricting the abundance of fish and the small sizes of marine invertebrates at this time. The presence of ooids and seafloor fan cements in our study sections indicates highly saturated conditions rather than acidification at the end of the Smithian.

Key words: Smithian-Spathian extinction; redox changes; carbon isotopes; Early Triassic

1. Introduction

Occurring in the shadows of the end-Permian mass extinction, the Smithian-Spathian (S-S) extinction was first recognized as a minor Early Triassic marine crisis by Hallam and Wignall (1997). It has subsequently been identified as a major extinction of nektonic taxa (Orchard, 2007; Stanley, 2009), which coincides with a peak of Early Triassic warmth that is likely one of the hottest intervals of the Phanerozoic (Sun et al., 2012). Many of the benthic victims of the S-S crisis were “disaster taxa” that had flourished in the aftermath of the end-Permian mass extinction (e.g., many species of *Claraia* bivalves and bellerophontid gastropods) (Chen, 2004; Kaim and Nützel, 2011). In Utah, the S-S boundary is marked by a distinct lithology change from ammonoid wackestone to bivalve wackestone-packstone and an extinction of 10 out of 11 Smithian conodont species (Solien, 1979). Amongst radiolarians the low diversity populations of Permian holdovers were devastated causing the group to reach the lowpoint of its long history: only 12 genera are known from the late Smithian (O’Dogherty et al., 2011). It is a similar story on land with communities reaching a diversity minimum (Irmis and Whiteside, 2012). The successful *Lystrosaurus,* that had dominated post-extinction terrestrial environments, may also die out at this time (Fröbisch et al., 2010).

The Smithian was a time interval of major disturbances in the global carbon cycle. Negative excursions, typically of ~7‰ to ~10‰ magnitude are frequently seen in both carbonate ($\delta^{13}C_{carb}$) and organic carbon isotopes ($\delta^{13}C_{org}$) (Payne et al., 2004; Grasby et al., 2012), suggesting enormous light carbon inputs and/or major re-organization of the global carbon cycles. This was followed by a positive $\delta^{13}C_{carb}$ excursion of comparable size beginning around the S-S boundary interval before a second, lesser negative excursion in the early middle Spathian (Sun et al., 2012).

The extinction losses and carbon isotope trends have been linked in several models. One invokes isotopically light carbon dioxide emissions associated with Siberian flood basalt volcanism (Payne et al., 2004). The consequent acidification pulse is envisaged to have caused the marine extinctions (Galfetti et al., 2008; Saito et al., 2013) whilst the warming trend went hand-in-hand with oceanic anoxia. The subsequent enhanced burial of isotopically light organic C in anoxic sediments would have generated the positive $\delta^{13}C$ trend seen across the S-S boundary (Galfetti et al., 2007). In contrast, Meyer et al. (2011) argue that the positive $\delta^{13}C_{carb}$ trend records increased productivity in the water column thereby generating a steeper surface to deep isotopic gradient. In a third alternative, Horacek et al. (2007) argue that the initial negative shift reflects the overturn of a previously well-stratified ocean water column causing the release of light dissolved inorganic carbon, derived from remineralized organic matter, into the upper water column. All three scenarios differ in their predictions of the relative timing of carbon isotope excursions and anoxia. The Galfetti et al. (2007) alternative sees anoxia developed as $\delta^{13}C$ values swing to positive values in the latest Smithian, the Meyer et al. (2011) alternative has anoxia peaking later as $\delta^{13}C$ reaches maximum values whilst the Horacek et al. (2007) model has peak anoxia much earlier (in the late Smithian) just prior to the minimum in $\delta^{13}C$.

The temporal relationship between marine anoxia and the $\delta^{13}C$ curve is clearly a subject of debate as is the relationship between redox changes and the S-S biotic crisis. We examine both topics here in a study of sections from the Nanpanjiang Basin of South China and aim to show the relationship between anoxia and $\delta^{13}C$ trends. A combined conodont biostratigraphic and carbon isotope study is used to generate an age model, in conjunction with a facies and petrographic analysis of depositional conditions. The recovery from S-S boundary environmental perturbations also reveals the development of extraordinary marine red-bed facies (Griotte) reminiscent of similar facies developed in the aftermath of other intense phases of oceanic anoxia in both the Devonian and Cretaceous.

2. Geological setting

In the Late Permian, the Yangtze Platform was situated at equatorial latitudes in the Palaeo-Tethys (Fig. 1A) and gradually rotated counter clockwise and moved northwards to ~12°N in the early Middle Triassic (Enkin et al., 1992; Lehrmann et al., 1998). The Nanpanjiang Basin was situated to the southwest of the Yangtze Platform, and was a deep water epicontinental basin (Fig. 1B) in which the Great Bank of Guizhou (GBG) was an isolated carbonate platform (Lehrmann et al., 2003).

A series of sections ranging from the Late Permian to Late Triassic are exposed around Jiarong Village and Bianyang Town (Guizhou Province) within the Nanpanjiang Basin. The studied section Jiarong III (25°55'17.12"N, 106°33'49.75"E; Fig. 2A) was situated between the southern edge of the Yangtze Platform and the northern margin of the GBG, representing a basin margin location. The other studied section at Mingtang (25°36'15.84''N, 106°38' 18.72''E), 4.5 km west of Bianyang Town, was situated at the northern edge of the GBG, representing an outer platform setting. Two additional sections at Jinya and Zuodeng (Guangxi Province) were also briefly examined for reference.

3. Methods

The two sections were logged in detail and 7-14 kg samples were collected for conodont extractions together with more abundant smaller samples for petrographic and carbon isotope analysis.

3.1 Conodont extraction

Conodont samples were crushed to small chips and dissolved by using 10%

acetic acid at China University of Geosciences (Wuhan). The acid solution was exchanged every 48 hours until the rock chips were fully dissolved. Residuals were wet sieved and dried at 50 °C in an oven. Sodium polytungstate heavy solution (2.81 g/cm^3) was used for density separations. The heavy fraction was washed with distilled water and dried at 50 °C. Conodonts elements were picked under a binocular microscope.

3.2 Thin-section, SEM and framboid pyrite analysis

Seventy four thin sections were examined using a petrographic microscope. Microfacies types are based on the petrographic features as well as macroscopic features of the sediments observed in the field. In addition, 30 polished blocks were examined using scanning electron microscopes equipped with energy-dispersive X-ray spectroscopy (SEM-EDS) under backscattered electron (BSE) mode at the University of Hull (UK) and the University of Hong Kong (China). Elemental mapping was performed to characterize the distribution of iron in the red lithologies. Where present, pyrite framboid diameters were measured at 2500X magnification under BSE mode.

3.3 X-ray diffraction (XRD)

X-ray diffraction (XRD) analyses were conducted to determine main mineral compositions in rocks. Measurements were performed on a Siemens D5000 X-ray diffractometer with CuKα radiation (λ = 0.154 nm) and a graphite secondary monochromator at the GeoZentrum Nordbayern, University of Erlangen-Nuremberg (Germany) (short as "Erlangen" below). Samples were ground to fine powders by using a mill and tightly packed into round tablets. The sample tablets were scanned from 2° to 65° for 2θ, with a step size of 0.02° and a counting time of 2 s/step.

3.4 Major elements (X-ray fluorescence-XRF)

Fresh samples were milled to fine powders and dried at 105 °C overnight. After determination of combustion loss, samples were melted into glass tablets and measured using a AMETEK Spectro XEPOS XRF analyzer at Erlangen.

3.5 Trace metals

Trace metals (molybdenum and uranium) concentrations were determined at the Isotope Science Laboratory, University of Calgary (Canada). Elemental determinations were carried out on powdered samples digested in a 2:2:1:1 acid solution of H_2O-HF-$HClO_4$-HNO_3. Solutions were analyzed using a PerkinElmer mass spectrometer. Reproducibility was better than ±2% (2σ).

3.6 Mössbauer spectroscopy

^{57}Fe Mössbauer spectroscopy is a powerful tool to determine the oxidation state and coordination of iron in bulk mineral compositions (e.g., Burns, 1994). Investigations were performed on a custom-built Mössbauer spectrometer at the University of Hong Kong. Fine sample powders were loaded in acrylic holders and measured in a transmission mode with a 25 m Ci^{57}Co/Pb gamma-ray source under constant acceleration at room temperature. The velocity scale was calibrated with a reference to the spectrum of α-Fe foil. Lorentzian doublets were used and the recoilless fractions of iron in octahedral and tetrahedral crystallographic sites were considered equal for fitting the areas of sub-spectra (Gorski and Scherer, 2010). Mössbauer hyperfine parameters: Fe(II)- IS=0.7-1.2 mm/s, Fe(III)- IS=0.3-0.6 mm/s.

3.7 Carbon isotope and total organic carbon (TOC) analyses

For $\delta^{13}C_{carb}$ analyses, carbonate powders were sampled using a micro-drill on fresh-cut rock surface. Sample powders were reacted with 100% phosphoric acid at 70 °C in a Gasbench II auto-sampler connected online with a ThermoFinnigan Delta V Plus mass spectrometer at Erlangen. All values are reported in per mil relative to V-PDB by assigning a $\delta^{13}C$ and $\delta^{18}O$ value +1.95‰ and -2.20‰ to NBS 19 and -46.6‰ and -26.7‰ to LSVEC, respectively. Reproducibility was monitored by replicate analysis of laboratory standards calibrated to NBS 19 and LSVEC, and was better than ±0.09‰ (2σ).

For measurements of $\delta^{13}C_{org}$ and TOC contents, samples were milled to fine powder and treated with 10% HCl at ~60 °C to remove carbonate components. Insoluble residues were washed with deionized water for at least 5 times, dried at 55 °C and homogenized using a mortar. $\delta^{13}C_{org}$ and TOC were analyzed using an elemental analyser (CE 1110) connected online to a ThermoFisher Delta V Plus mass spectrometer. Reproducubility of the analyses was better than ±0.06‰ (2σ) for $\delta^{13}C_{org}$ and 0.09% (2σ) for TOC.

4. Conodont biostratigraphy

Detailed studies of the conodont biostratigraphy for the Lower Triassic strata of the Jiarong area were provided by Chen (2011). During this study, additional samples were collected. This enabled the *Novispathodus waageni*, *Discretella discreta* and *Parachirognathus -Pachycladina* zones to be established indicating a middle-late Smithian age whilst the *Nv. pingdingshanensis*, *Icriospathodus collinsoni* and *Triassospathodus homeri* zones are established for the Spathian (Fig. 3).

At Mingtang we recognised three zones, despite exceptionally low conodont yield rates (commonly 1~3 elements per 10 kg rock). They are, in ascending order, *Tr. symmetricus* Zone, *Tr. homeri* Zone and *Nv. triangularis* Zone (Fig. 4). The *Tr. symmetricus* Zone is established for the early Spathian and is correlated to the upper part of *Ic. collinsoni* Zone at Jiarong, due to the absence of *Ic. collinsoni*. The S-S boundary interval is either not exposed or cut-out by faulting. A massive dolomite unit represents the lowest part of the late Smithian (?) sediments and the contact with the overlying dark grey, laminated/nodular marls and micrites is irregular and partially obscured, suggesting a gap in the section.

Overall the two sections show a slight overlap in their stratigraphic range. The Jiarong III section straddles the S-S boundary whilst the sediments of the Mingtang section are of Spathian age and the presence of *Tr. brochus* at the top of the section suggests it extends to late in this substage.

5. Lithology and facies

Based on field features and petrographic analysis, 7 facies were identified in the sections.

5.1 Black shale

Black or grey-brownish shales are developed at Jiarong and Jinya. The Jiarong III section was freshly exposed, due to building excavations. Thus, the brown-coloured variant of "black shale" in the latest Smithian is considered to be the original depositional colour rather than a weathered version of the black shale. In thin sections the shales are laminated on a sub-millimeter scale and lack any fossils. At Jinya, pyrite framboids are very abundant in the black shales; in addition, cm-size pyrite cubes occur in the interbedded limestones.

5.2 Banded (alternating) wackestone and marl

This very common facies consists of centimetre-scale alternations of wackestone (or sometimes micritic mudstone) and marl (Fig. 2D). Lamination is present at some levels whilst more massive developments of the facies are caused by thorough bioturbation. The effect of burrowing is clearly demonstrated in the intervals where the marls are typically red and the wackestones are white while the burrow fills show contrasting colour with host rocks. The colour contrast provides an excellent opportunity to investigate the bioturbation, which consists of millimetre-diameter burrows that include both vertical “micro-*Skolithos*” and horizontal “micro-*Planolites*” (Fig. 5A, B). At no level does the bioturbation succeed in homogenizing the original centimetre-scale bedding suggesting that intense burrowing by larger organisms was never present. However, at some levels the beds become discontinuous and nodular in appearance, which is probably due to bioturbation (Fig. 5C).

The red limestones are grouped into a unit informally called the “Griotte Unit”, best observed at Mingtang. Griotte is a term applied to nodular, red micrites that were widespread in deeper water settings of the Famennian (Late Devonian), when they developed after the Kellwasser anoxic events (Boyer, 1964). We suspect the Spathian Griotte beds to have similar significance to their Devonian counterparts (discussed in Section 6) and as such we use the term here to describe similar reddish units.

Fossils are common in the non-laminated wackestones and include ostracodes, thin-shelled bivalves and several types of calcispheres. The bivalves are typically articulated and filled with sparry cement suggesting a low energy environment. In some cases, the exterior of the shells reveals an overgrowth of radial crystals with irregular thickness reminiscent of fans of seafloor cement common elsewhere in the Early Triassic (Fig. 6G; Woods et al., 2007). Fossils are much rarer in the laminated beds but tiny pyrite grains are common.

5.3 Dolosparite

Beds of dolostone comprised of silt-sized rhombs are relatively common, notably at Jiarong III. Where vestiges of original (unaltered) lithology are seen, the precursor lithology is micritic mudstone suggesting the dolosparite is a product of diagenetic alteration of the banded wackestone/marl facies.

5.4 Filamentous wacke-/ packstone

Thin-shelled bivalves dominate this rare facies with most valves aligned parallel to bedding. The majority of valves are flat and often fragmented although more convex valves also occur. Other grains include peloids and pyrite (Fig. 6A).

5.5 Pelsparite/calcarenite

Well-sorted, sand-grade peloids dominate the components of this facies. Occasionally the peloids contain calcispheres indicating that in some cases they are highly abraded intraclasts of calcisphere wackestone. Other clasts in this facies include ostracodes, echinoderms, superficial coated grains, composite ooids and rare pisoids (Figs. 6B, D, H and 7A, B).

Calcarenite beds are typically ~30 cm thick, with sharp, planar bases. Occasionally they show grading and have upper surfaces that are hummocky.

5.6 Intraclast Breccia

Intraclast breccia beds are present at both Jiarong, where bed thickness is < 1 m, and at Mingtang where this facies is more common with individual beds reaching thicknesses of up to 6 m. Clasts types are diverse and are derived from all the other facies types described above, including black shale (Fig. 2D). Typical clasts are angular and irregular in shape although those derived from the banded wackestone/marls are often tabular. Clasts are poorly sorted and show a wide range of sizes within the beds. The maximum clast size correlates with bed thickness. Thus, beds <2 m thick have some clasts approaching 40 cm in size whilst the thickest bed (6 m thick, seen at Mingtang) has a peak clast size >1.4 m in maximum dimension.

Most clasts "float" in a micritic matrix, which is commonly altered to dolosilt, and occur in beds that lack any structure or internal organization. However, there are some intriguing exceptions. A 1 m thick bed found 8 m above the base of the Mingtang section (Fig. 4) reveals a well-sorted, clast-supported basal level composed of clasts a few centimeters in size, which grades up into a more typical matrix-supported breccia with a greater range of clast sizes. A 50 cm-thick bed at the 22 m level at Mingtang shows imbrication of tabular clasts at its base but chaotically oriented clasts above. Both these horizons suggest considerable variation of the flow regime beginning with a traction carpet of clasts before developing into high-concentration debris flows.

5.7 Flat Pebble Conglomerate (FPC)

Flat pebble conglomerate beds, composed of intraclasts, are common in both sections and differ significantly from the intraclast breccias. Clast sizes are smaller and less variable, typically ranging from a few millimetres to several centimetres. Most clasts are eroded from the banded wackestone facies (Fig. 6C), which explains their consistent "flat pebble" morphology. Beds are also of more consistent thickness, typically ~40 cm, and never exceed one metre thickness. Clast density is also much greater; all FPC beds are clast supported with the great majority of clasts lying bedding parallel (Figs. 2F, 6C). In a few cases normal grading (fining upward) is seen but in most beds the clast size is uniform throughout the bed.

6. Iron petrography, trace metal variations and redox trends

Framboids are common in all lithologies at Jiarong below the Griotte Unit.

Mean framboid diameters are generally between 5~7 μm, typical of dysoxic conditions but framboids from the banded wackestone/marl facies in the *Parach.-Pachy.* and the basal *Nv. pingdingshanensis* zones have smaller sizes indicating anoxic conditions (Fig. 3, Table 1). Interestingly this indicates that the most intensely anoxic intervals were immediately prior to the onset of black shale deposition in the latest Smithian, and again immediately above the S-S boundary. These observations are supported by redox-sensitive trace elements that show increases above average shale values in the same intervals (e.g., Mo>1 ppm; U>3 ppm).

Framboids are much rarer at Mingtang indicating much better oxygenation levels. Only three samples yielded sizable populations of framboids (Fig. 7). Mean framboid diameters ranged from 6.3 to 7.4 μm, typical of dysoxic conditions. These are from the early Spathian Carbonate Unit I, and one sample each from the FPC facies in the Griotte Unit and the upper Carbonate Unit II. The framboids are only concentrated in the flat pebbles in the Griotte Unit. Likewise, redox sensitive trace elements remain below average shale values throughout the section (in most samples Mo<1 ppm, U<1.5 ppm).

Collectively, oxygen-starved conditions began in the late Smithian and extended into the earliest Spathian. They are frequently developed in the laminated, framboid-rich banded wackestone/marl in the *Parach.-Pachy.* Zone as well as in black shale facies in the *Nv. pingdingshanensis* Zone. At the latter level oxygenation varied dramatically because the lowermost Griotte beds are interbedded with the black shales (Figs. 2C). The griotte-dominated Mingtang section was largely oxic, with only sporadic dysoxia.

The Griotte Unit forms a distinctive part of the Spathian stratigraphy in both study sections and extend upwards to higher stratigraphic levels. The red colour is confined to fine-grained sediments and consequently many of the intraclast breccias consist of distinctive white clasts floating in a red, fine-grained matrix (Fig. 5A). The transition between red and grey coloured strata is always bedding parallel rather than (for example) along joint surfaces suggesting it was an original sedimentary colour and not produced by later oxidizing groundwater (Fig. 5A, B). The boundary between red and grey facies is also typically sharp, either occurring over a few millimetres or across the span of a bedding plane (Fig. 5E). Remarkably, red micrite can be in sharp contact with pyrite-rich black shale facies suggesting abrupt changes in redox conditions (Fig. 2C).

XRD investigations on bulk samples from the Griotte Unit show that the reddish levels have a major mineral composition of calcite, dolomite (ankerite), quartz and a small proportion of clay minerals such as kaolinite and clinochlore. Muscovite may also occur in some levels. There is no significant difference in mineral composition between the Griotte Unit and underlying beds. Iron concentration is also low (generally <1%) and decreases upsection (Fig. 4; Table 2). EDS-BS-SEM examinations on polished surfaces of Griotte limestone/marl reveal that non-carbonate minerals are mainly apatite, iron-oxides, Fe-Ti oxides, “pyrite” framboids, quartz, rutile, zircon and occasionally rare earth element-rich minerals (Fig. 8A-C). Iron oxides are not detected by XRD, due to the low content but were revealed by SEM-EDS as finely disseminated iron oxide particles <1 μm or larger mineral grains ~15 μm in size (Fig. 8A-C, E). ^{57}Fe Mössbauer spectroscopy indicates that hematite is the main iron-bearing phase in the Griotte facies, composing ~40-50% of all iron-bearing minerals. Other mineral phases include Ti-Fe oxides, carbonates, silicates and trace amounts of sulfides (Fig. 8F). Despite its low concentration, the presence of the ultra-fine iron oxides is considered sufficient to impart the bright reddish pigmentation to the rocks (Fig. 8E).

7. Paleontology

Benthic fauna is locally common and dominated by thin-shelled bivalves and ostracodes with rarer echinoderm grains, foraminifera and very rare microgastropods. The Griotte Unit is bioturbated but contains few shelly fossils.

7.1 Conodonts

The S-S conodonts in the Nanpanjiang Basin generally show a very low diversity compared to coeval faunas from higher latitudes. Three genera, namely *Neospathodus* (*sensu lato,* including *Novispathodus, Triassospathodus*), *Parachirongnathus* and *Icriospathodus*, are most commonly seen. *Neospathodus* is the dominant genus from the early Smithian to the late Spathian (Fig. 9), whilst the *Parachirognathus/Pachycladina* group was only briefly dominant in the late Smithian. *Icriospathodus* only occurs in the early-middle Spathian. Gondolellids (*sensu stricto*) are, if present at all, always a minor component amongst conodont populations. They are entirely absent in the Smithian and only appear in the *Ic. collinsoni* zone. In contrast, late Smithian *Scythogondolella* is the common and dominant genus in North America, the Canadian Arctic and Spitsbergen (Paull, 1983; Orchard and Zonneveld, 2009).

Oxygen isotope analyses suggest that the neogondolellids lived in deeper water than *Neospathodus sensu lato* (Sun et al., 2012). The development of an oxygen-poor deeper water column in the Smithian may therefore account for their absence/rarity at this level.

7.2 Fish

No fish body fossils are found in our study despite the prevalence of dysoxic-euxinic facies favorable for their preservation. However, fish diversity/abundance data can be assessed because they are a common “by-product” of conodont extraction. Remarkably our study yielded few fish remains from the conodont residues despite the processing of large samples weighing 7-14 kg. In contrast, late Permian (and Middle/Late Triassic)-age samples of comparable weight and facies yield many more fish teeth than conodonts (e.g., Youngquist, 1952).

At Mingtang, fish remains are entirely absent in the lower Spathian strata but appear upsection. Thus, four small fish teeth are found in a late Spathian sample (*Nv. triangularis* Zone). Three of them are small cone teeth from bony fish (300-500 μm in height) and the other is from the chondrichthyian *Hybodus* – a tooth ~2 mm in length. More than 500 kg of Griesbachian to Spathian samples from Jiarong were processed. They yielded 1874 conodont elements and only 7 fish teeth, 5 out of which came from the *Ic. collinsoni* and *Tr. homeri* zones of the middle-late Spathian.

7.3 Foraminifers

Foraminifers are mostly encountered in the Spathian Griotte Unit at Mingtang, but only occur at 3 levels at Jiarong (Table 3). At Mingtang, the most common taxa are *Hemigordiellina regularia*, and *Meandrospira pusilla*, while *Earlandia*, *Rectocornuspira kahlori*, *Hoyenella* spp., and *Globivalvulina lukachiensis* are also present at several levels in the Griotte Unit. They are mostly 100-300 μm in diameter. In contrast, foraminifers at Jiarong are exceptionally rare, and very small, being generally less than 100 μm in diameter. *H. regularia*, *M. pusilla*, and *R. kahlori* are present in the Smithian Carbonate Unit. Only *H. regulari* and a questionable globivalvulinid are recorded in the Spathian, at the top of the Black Shale Unit.

Collectively, foraminifers were very small, simple and rare at the S-S boundary interval (Fig. 3). Their diversity shows a steady increase in the middle-late Spathian (Fig. 4). However, at no level does any sample contain more than 3 genera.

8. Carbon isotope chemostratigraphy and total organic carbon (TOC) content

The $\delta^{13}C_{carb}$ data from Jiarong show large perturbations (Fig. 3), consistent with earlier studies of this interval (e.g., Payne et al., 2004; Horacek et al., 2007). Values are relatively stable in the late Smithian albeit with a minor negative excursion from -2.2‰ to -3.4‰ in the *Ds. discreta* and *Parach. -Pachy.* zones of the late Smithian. This represents the nadir of the longer-term ~-8 to -10‰ Smithian negative $\delta^{13}C$ excursion (Fig. 2B). A rapid ~+7‰ positive excursion is recorded from the latest Smithian to earliest Spathian, coincident with the onset of black shale sedimentation at Jiarong III. Analyses of $\delta^{13}C_{org}$ show a similar positive excursion with the same amplitude (Fig. 3), suggesting a co-variation of carbon isotope compositions in both the inorganic and organic carbon. This is followed by a ~-4.5‰ negative excursion in the early Spathian. Thus, $\delta^{13}C$ values decrease from +4.1‰ in the lower *Nv. pingdingshanensis* Zone to -0.2‰ in the uppermost *Ic. collinsoni* Zone coincident with the gradual suspension of organic-rich sedimentation, recorded in the uppermost Black Shale Unit, and the development of the Griotte Unit. This positive trend is seen at the top of the Jiarong III section and is picked up at the base of the Mingtang section where values reach a low point of -1.2‰ in the middle of *Tr. homeri* Zone (Fig. 4; Fig. 10) before rising to values of 0.8‰ in the highest sampled level in the *Nv. triangularis* Zone of the late Spathian.

TOC values measured on shales and limestone lenses in the lower Black Shale Unit at Jiarong III show a decrease from ~1.1 – 1.5% in the black shales of the late Smithian to ~0.3-0.5% in the brown shales that are immediately below the S-S boundary.

9. Discussion

9.1 Facies interpretation and stratigraphic trends

The facies at Jiarong and Mingtang records a considerable range of depositional conditions. The black shale and banded alternating wackestone/marls facies represent low-energy hemipelagic sediments and it is likely that the filamentous packstones are of similar origin. In contrast, the calcarenite facies records prolonged winnowing and sorting suggesting a persistently high-energy environment. The sharp-based nature of the calcarenite beds may record storm events that transported material down slope from higher energy, shallower waters settings.

In contrast, both the intraclast breccias and the FPCs contain material that was sourced *in situ*, within the sections. This observation, together with the often-angular nature of the clasts, suggests erosion and down-slope transportation during a single event. Such events must have had considerable erosive power because they were capable of eroding and transporting blocks in excess of a metre in diameter. For some beds the flow regime varied substantially during emplacement. In a few cases the presence of traction-related basal layers, such as imbricate flat pebbles, indicates an early phase of relatively low-density, poorly cohesive flow prior to the emplacement of much higher-density, cohesive debris flow deposits (matrix-supported breccia). This evolution of flow style is reminiscent of hybrid event beds, often known as linked debrites, recorded from clastic turbidite systems (Haughton et al., 2009), although our coarser and thicker carbonate examples contain a much greater debris flow component.

FPCs are common carbonate facies prior to the Ordovician and become rarer afterward (Sepkoski et al. 1991), although they are common in the Early Triassic Wignall and Twitchett, 1999; Woods, 2014). FPCs have been generally interpreted as a storm facies caused by the break-up of partially lithified, thin-bedded sediment during storm events followed by transport (Wignall and Twitchett, 1999). However, common features of other FPC beds, such as edgewise stacking and imbrications, are lacking from our S-S examples. The alignment of flat clasts with bedding suggests settling from suspension of a low cohesion flow. In this regard they are probably of similar origin to the basal layers seen in some of the intraclast breccias. The FPCs and breccias could both be the product of the same sequence of events: seafloor erosion (by storms) followed by down-slope movement of sediment gravity flows. They may only differ in the nature of the transported material: the FPCs only incorporating small, flat pebbles whilst the breccias involved the entrainment of considerable amounts of micrite mud that ensured much higher concentration flows.

Overall Mingtang has a much higher proportion of event beds (pelsparites, intraclast breccias and FPCs) than Jiarong suggesting it may be more proximal. The clearest water depth indicator occurs at the levels in the Spathian where hemipelagic facies are lost and pelsparites (the highest energy facies) dominate. This suggests shallowest conditions are found during the early Spathian in the *Ic. collinsoni* Zone (Fig. 3) and at the top of study interval in the *Nv. triangularis* Zone.

9.2 A Smithian-Spathian anoxic event

Oxygen-depleted facies straddle the S-S boundary at Jiarong III, as shown by the abundant small pyrite framboids as well as redox sensitive trace elements at these levels. A prolonged phase of anoxia began in the late Smithian. True organic-rich shales only occur in the *Parach. -Pachy.* Zone of the latest Smithian and (in thin beds) in the *Nv. pingdingshanensis* Zone. Intriguingly these "black shales" yield slightly larger framboids, suggestive only of dysoxic conditions. The smallest framboids are found in interbedded wackestones immediately above the stage boundary.

Black shales are geographically widespread in the latest Smithian, recording enhanced organic matter burial accompanying anoxic-euxinic conditions. For example, Chen et al. (2011) record laminated carbonates, a probable anoxic facies, from the latest Smithian of the Chaohu region. Similar organic-rich sediments associated with oxygen-poor conditions have been reported in the Nanpangjiang Basin (China), Japan, Vietnam and the Russian Far East (Galfetti et al., 2008; Shigeta et al., 2009; Komatsu et al., 2014). Further afield and contemporaneously, intense euxinia is developed in the Smithian Stratotype in the Sverdrup Basin, Canada (Grasby et al., 2012), whilst the overall oxygen-poor Early Triassic history of the Panthalassa Ocean shows an intensification of anoxia in the late Smithian sedimentary record of Japan (Wignall et al., 2010).

9.3 Anoxia and $\delta^{13}C_{carb}$ oscillations

The trends and magnitude of the $\delta^{13}C_{carb}$ values at Mingtang and Jiarong III closely match other inorganic (Payne et al., 2004) and organic (Grasby et al., 2012) $\delta^{13}C$ records, and independently confirm our conodont age dating (Fig. 10). The detailed record of oxygenation trends also helps to evaluate the proposed models for oceanographic changes. The onset of the positive shift in $\delta^{13}C_{carb}$ in the latest Smithian coincides precisely with the onset of black shale deposition (although anoxic conditions had begun earlier). It could therefore be argued that the widespread and enhanced burial of isotopically light organic matter was responsible for the coincident positive excursion in $\delta^{13}C_{carb}$ as suggested by Galfetti et al. (2007).

Alternatively the positive excursion has been ascribed to increasing surface water productivity creating a steeper $\delta^{13}C_{carb}$ gradient within the water column (Meyer et al., 2011). In this scenario the organic carbon enrichment is due to high surface water productivity. However, $\delta^{13}C_{carb}$ values only reflect the changes of isotopic composition in the dissolved inorganic carbon pool in the upper water column where most carbonates are formed. Changes in $\delta^{13}C_{carb}$ alone cannot determine whether this positive trend is due to enhanced primary productivity exporting ^{12}C from the photic zone or due to enhanced organic carbon burials in the sedimentary reservoir (e.g., Joachimski, 1997).

Comparison of the $\delta^{13}C_{carb}$ values of our relatively shallow-water site at Mingtang and the deep-water settings such as Zuodeng and Jinya (Sun et al., 2012; Fig. 10) suggest that the middle-late Spathian ocean had a $\delta^{13}C_{carb}$ gradient similar to the modern Bahama Bank where values from the platform are lighter, due to higher organic carbon remineralization rates (e.g., Patterson and Walter, 1994; Fig. 11). This contradicts the prediction of the Meyer et al. (2011) model that $\delta^{13}C_{carb}$ from shallow water sites should be heavier than coeval values from deep-water settings.

In a third alternative, Horacek et al. (2007) argue that the exceptionally large, -6‰ negative shift in $\delta^{13}C_{carb}$ in the Smithian reflects the overturn (and oxygenation) of a well-stratified water column releasing isotopically light carbon. This scenario receives no support from the redox/sedimentary history of the Nanpanjiang Basin, nor other studies, which show increasing euxinicity as well as enhanced organic carbon burial in many global settings in the late Smithian.

In summary, the close link between the onset of anoxia in the latest Smithian of South China and a reversal of $\delta^{13}C$ trends from lighter to heavier values lends credence to the notion that enhanced organic carbon burial rates are the main control of the positive $\delta^{13}C$ excursion in the latest Smithian.

9.4 Griotte Units

Perhaps the most extraordinary facet of the Smithian-Spathian strata of the Nanpanjiang Basin and elsewhere are the Griotte Units developed in the early Spathian. The occurrence of coeval red claystone in the deep-sea sediments in the middle of Panthalassa (e.g., Takahashi et al., 2009) argues against a detrital provenance of the red colour. Interestingly, this red pigmentation is clearly associated with the "Iron Paradox": Fe(II) (ferrous ion) is soluble in seawater but only stable in anoxic environments, whereas Fe(III) is much less mobile (insoluble in seawater) and predominates in oxic, surface water. Thus development of Griotte facies at the sea floor requires extensive oxygenation of Fe(II) that only exists in reducing environments. The question is how to oxygenate/ventilate an anoxic and potentially stratified ocean.

Our analysis shows that the reddish pigmentation is due to trace amounts of ultra-fine grained (<1 μm) iron oxide particles (i.e., hematite) dispersed amongst the micrite muds (Fig. 8E). These hematite particles are the stable phase transformed from the most reactive phase, Fe(oxyhydr)oxides. Fe(oxyhydr)oxides nano-particulates form in sea waters where 1) Fe(II) in reducing environments mix (and react) with an oxic water mass and 2) oxidation of Fe(II)-bearing minerals (carbonate, silicate, sulfide etc.) (Raiswell and Canfield, 2012).

In normal marine settings such fine material would be highly reactive and involved in the oxidation of organic matter. That the tiny grains survived diagenesis and later burial suggests very organic poor/well oxygenated conditions. Stable carbon/oxygen isotope analyses at the contact between the Griotte limestone and the grey limestone show no variations at this change in redox conditions (Fig. 5F). Even more remarkable, the oldest Griotte facies are closely interbedded with organic-rich shale with abundant pyrite framboids (Fig. 2C) pointing to depositional conditions that alternated from highly reducing to highly oxic on short timescales.

Red marine sediments of Spathian age are also known from deeper water settings in China and elsewhere (Fig. 1A), although they are most commonly < 10 m in thickness and restricted to the *Ic. collinsoni* conodont zone (e.g., in Jiarong and Zuodeng). The *Ic. collinsoni* Zone is correlated to the *Columbites* ammonoid zone (Sweet et al., 1971), representing an early Spathian age. The Griotte development is alternatively assigned to the *Ic. crassatus* or *Tr. homeri* conodont zone because of absence of *Ic. collinsoni* and/or coarser conodont biostratigraphic schemes (e.g., Wang et al., 2005).

In most shallow-water sections, the Griotte develops around the *Ic. crassatus* zone and lasts until the *Tr. homeri* zone of the middle-late Spathian (e.g., Mingtang, this study; Guandao, Wang et al., 2005). In South Tibet red limestones and shales ("Ammonitico Rosso" facies) are known in the early-mid Spathian (Garzanti et al., 1998). Similar Spathian red shales/claystones are known from the deep sea sediments in Japan (Takahashi et al., 2009).

The Griotte facies have also been recorded in the aftermath of other widespread anoxic events. For example, red marine shales are found immediately following widespread black shale deposition in the Early Silurian (Ziegler and McKerrow, 1975). The "Vrai Griotte" is another example developed after the Late Devonian twin-phased anoxia of the Kellwasser facies (e.g., Préat et al., 1999; Bond et al., 2004). Deep-ocean red beds are also widespread during the Turonian (Late Cretaceous) following the Cenomanian-Turonian (C-T) oceanic anoxia (Wang et al., 2011). Models to explain the formation of these Cretaceous strata may be applicable to the Spathian Griotte Unit.

The model of Wang et al. (2011) for the Cenomanian-Turonian works thus: oceanic anoxia enhances the burial of organic matter and pyrite thereby liberating large amounts of oxygen to the atmosphere and drawing down atmospheric carbon dioxide levels. The cooling trend improves ocean circulation and the increased oxygen availability improves dissolved oxygen levels. Thus, the oceans become better oxygenated allowing increased iron oxide burial along with phosphorus burial. This process increases ocean circulation but does not lead to increased nutrient input to shallow waters via upwelling because scavenging of phosphorous by sinking iron (hematite) particles is enhanced. Consequently, the increased oxygenation and diminished nutrient availability creates a well-ventilated, low productivity ocean in which organic matter remineralization is minimal, allowing fine particulate iron oxides to survive diagenesis.

There are several similarities between the C-T and S-S events besides the post-anoxia red beds: both show widespread black shale deposition during peaks in global warmth and both were followed by loss of anoxia during a cooling trend. In fact, the basic gist of this model, in which oceanic anoxia is self-limiting due to carbon dioxide drawdown and cooling, is well known and long established (e.g., Joachimski and Buggisch, 1993). The model of Wang et al. (2011) is in effect a more extreme version in which the oxic rebound is exacerbated by exceptionally low primary productivity in a nutrient-starved ocean. Interestingly, in both cases it is the first phase of widespread anoxia and high temperatures that coincides with extinctions, and not the low productivity but well ventilated aftermath.

Alternatively, the red pigmentations could be attributed to iron bacterial activities, which could produce submicronic hematite in dysoxic conditions during the early diagenesis. This is suggested for the Jurassic Ammonitico Rosso limestones in Italy (Préat et al., 2011). However, typical features of this scenario such as ferruginous microstromatolites and iron hardgrounds are not seen in our Early Triassic samples. In more extreme circumstances such as ferruginous oceans with low sulphate concentrations, hematite could form, without the presence of free oxygen, through photochemical pathways or by anoxygenic phototrophic bacteria (e.g., Francois, 1986; Keppler et al., 2005). However, such conditions are not widely known in the Phanerozoic and the interbedded black shales contain abundant pyrite.

9.5 Extinction mechanism of the Smithian-Spathian crisis

Ocean acidification is a popular extinction mechanism for the S-S marine biotic crisis (Galfetti et al., 2008; Saito et al., 2013), but we highlight that the widespread development of marine anoxia (discussed above) is likely to have been a significant cause of the extinction. We also note the evidence for carbonate supersaturation in the later Early Triassic (e.g., Pruss et al., 2005) does not support arguments for acidified oceans. Anoxic oceans could be more homogenously saturated because of bicarbonate production by anoxic remineralization, which in effect supresses $CaCO_3$ dissolution and promotes $CaCO_3$ precipitation on the seafloor (Higgins et al., 2009). In our study, ooids are common throughout the sections in the pelsparite facies (Fig. 6D, I-K) and the development of seafloor fans on bioclasts (Fig. 6G) indicates carbonate supersaturated conditions in the S-S interval.

It has recently been shown that the S-S boundary coincides with a peak of sea-surface temperatures through the Late Permian – Middle Triassic, with equatorial values in excess of 40°C (Sun et al., 2012). Comparison with modern temperatures thresholds shows such values would be hostile for many marine organisms (Allen et al., 2002; Pörtner & Knust 2007; Sharp et al., 2014). Equatorial fish are considered likely to be especially vulnerable to temperature increases in the coming century (Cheung et al., 2013) and the rarity of fish remains in our study, from an equatorial setting, could reflect such a high temperature-controlled elimination.

It is well known that high temperatures also cause organisms to shrink in size (e.g. Allen et al., 2002; Peck et al., 2009; Cheung et al., 2013) and we note that all the fossils and trace fossils seen in the Nanpanjiang strata are exceptionally small. For example, most Smithian-Spathian foraminifers are ≤100 μm in diameter whereas those taxa also present during other intervals were consistently larger. Thus, Carboniferous *Rectocornuspira* are typically >200 μm in width (e.g., Cózar et al. 2008) and in the latest Permian *Hemigordiellina* approach 400 μm (e.g., Angiolini et al., 2010) whilst *Globivalvulina* are typically 250 μm in diameter (e.g., Nestell et al., 2011). Other factors such as low oxygen levels can be responsible for small size but in this case the small foraminifers are found in the well-oxygenated Griotte facies of the Spathian.

It is likely that the exceptional warmth at the S-S boundary was a critical factor, along with anoxia, in the extinction mechanism (Sun et al., 2012; Song et al., 2014). Indeed it is significant that the higher oxygen needs of marine organisms at higher temperatures makes them especially vulnerable to dysoxic conditions (Pörtner, 2010).

10. Conclusions

The studied sections from the Nanpanjiang Basin record both hemipelagic and storm-influenced deposition. Changes in facies and redox conditions are constrained by our high-resolution $\delta^{13}C$ chemo- and conodont biostratigraphy. A range of event beds are seen, including flat pebble conglomerates and breccia debrites that bear similarities to the hybrid event beds seen in clastic turbidite successions albeit with much thicker debrite intervals. Convincing evidence for shallowing, manifest as the loss of fine-grained facies and development of grainstones, is seen in the early-middle Spathian as well as late Spathian (upper *Ic. collinsoni* Zone and *Nv. triangularis* Zone).

Anoxia was widespread in this storm-influenced setting during the late Smithian and persisted into the earliest Spathian (last seen in the *Nv. pingdingshanensis* Zone at Jiarong). This was followed by a rapid transition to the exceptionally well-ventilated conditions recorded by marine red beds. The reddish pigmentation is derived from nano-particles of hematite. Their preservation suggests there was minimal remineralization of organic matter in the Early Spathian ocean.

The Spathian marine red unit, informally called the Griotte Unit, shows a form of "oxic rebound" from the anoxic-euxinic waters of the S-S interval. This may have been triggered by climatic cooling and oxygen increase driven by organic carbon and pyrite burial. The balance between euxinic and oxic conditions was a delicate one in the early Spathian. The timing of anoxia and $\delta^{13}C$ oscillations favour a model in which the late Smithian switch from a negative to a positive trend in $\delta^{13}C$ is best explained by increased burial of organic matter.

Anoxia, together with high temperatures, is postulated to have played a role in the S-S biotic crisis, while the latter factor also responsible for the exceptionally small size of foraminifers in the Griotte Unit and also the extreme rarity of fish throughout the Smithian-Spathian study interval.

Acknowledgements

Y.D. Sun acknowledges the Alexander von Humboldt Foundation for the fellowship. D. Lutz, S. Krumm, M. Potten (Erlangen) and Z.T. Zhang, H.S. Jiang (Wuhan) are thanked for lab and field assistance. J. Peakall (Leeds) and A. Munnecke (Erlangen) are thanked for discussions on the sedimentology. S. Pruss and an anonymous reviewer provide constructive comments. This study is supported by the Chinese Fundamental Research Funds for the Central Universities (CUG130615), 973 Program (2011CB808800), Natural Science Foundation of China (41272044), German Science Foundation (JO 219/14-1) and British Natural Environment Research Council (Advanced Fellowship Grant NE/J01799X/1).

Figure and Table Captions

Fig. 1. A., Early Triassic palaeogeographic reconstructions of Pangea and Panthalassa, modified from Muttoni et al. (2009). The Spathian Griotte facies are

widely distributed but are not known from the Boreal Ocean (Yin et al., 1992, Garzanti et al., 1998; Takahashi et al., 2009; Li et al., 2007 and this study); B., Relative positions of the Yangtze Platform, Nanapanjiang Basin and Qinling Trough; C., Palaeogeographic reconstruction of the Nanpanjiang Basin, after Lehrmann et al. (2003).

Fig. 2. Field photos of studied sections and biostratigraphic summary of Jiarong area. A., Field photograph of the middle and upper part of the Jiarong III section, showing 3 distinctive lithological units across the S-S boundary interval; B., Summary of the stratigraphic succession, conodont zones and the carbon isotope record of the Jiarong area. Conodont zonation is from Chen et al. (2013), carbon isotope data are from Sun et al. (2012); C., The lowermost part of the Griotte Unit at Jiarong III. Ruler is 35 cm in length; D., Intraclast Breccia facies overlain by thin-bedded Banded Wackestone and Marl facies at Jiarong III. The blue arrow points to large, black shale clast. Ruler is 40 cm in length; E., The Griotte Unit at Mingtang showing red-coloured wackestones, micrites and a flat pebble conglomerate bed; F., Flat pebble conglomerate bed in the lower Griotte Unit, Mingtang; Pebbles range from less than 1 cm to 30 cm in size. Conodont abbreviations: *Ic.=Icriospathodus*; *Nv.=Novispathodus*; *Parach.=Parachirognathus*; *Tr.=Triassospathodus*.

Fig. 3. Log of Jiarong III section with conodont and foraminifer ranges, the carbon isotope record, trace metal concentrations and pyrite framboid box-and-whisker plots (whereby the 'box' depicts the 25th and 75th percentile of framboid distributions, the 'whiskers' depict the minimum and maximum framboid diameters, and the central line the median average). Brown and orange dashed lines represent Mo and U concentrations in average shale, black dashed line shows Mo/Al ratio. Note that black shales change to brown shales in the latest Smithian. Conodont zonations are combined from data in Chen (2011) and Chen et al. (2013).

Fig. 4. Log of shallow water Mingtang section with conodont and foraminifer

ranges, the carbon isotope record, pyrite framboid box-and-whisker plots, Fe and Mo, U concentrations and Mo/Al ratio (see Fig. 3 caption for explanation). The $\delta^{13}C$ record shows smaller excursions (from 0.7‰ to -1‰) compared to most open water sections (e.g., from 3‰ to 0.5‰, Sun et al. 2012).

Fig. 5. Features of the Griotte Unit. A., Hand specimen showing small vertical and horizontal burrows (arrows), the coin is 1.5 cm in diameter; B., Polished slab of Griotte limestone (MT 19), showing both vertical "micro-*Skolithos*" and horizontal "micro-*Planolites*"; C., Banded (alternating) wackestone and marl facies, beds become discontinuous and nodular in appearance; D., Hand specimen of Griotte limestone, showing early Spathian bioclasts [consisting of unusually small ammonoids (A), bivalves (B) and scaphopods (S)] developed in the aftermath of the S-S crisis; E., Thin section photo, showing the sharp, undulatory contact between griotte and grey limestone; F., Polished slab of the Griotte limestone showing the grey-greenish micrite in contact with red micrite. $\delta^{13}C_{carb}$, sampled with a small dental dill, show no significant changes across the contact; G., a photomicrograph of the Griotte limestone shown in D, molluscan wackestone with cephalopod/bivalve shells, thick-shelled ostracodes, calcispheres and rare peloids. The ostracode shows both external encrustation (white arrow) and fringing bladed cements of variable thickness (black arrow).

Fig. 6. Carbonate thin-section photographs of Jiarong and Mingtang sections. A., filamentous wacke-packstones; B., pelsparite with dark round peloids and thin bivalve shells. Note the thick micritic envelope that has developed on the shell (blue arrow); C., flat pebble conglomerate (FPC) fabric from the Griotte Unit. Most pebbles are calcisphere wackestones except one (black arrow) which is a peloidal packstone with thin-shelled bivalves, crinoids and foraminifers; D., Superficial ooid with a peloid nucleus. The peloids are darker and finer-grained than the matrix suggesting aggrading neomorphism of the latter; E., A small benthic

foraminifer (*Hemigordiellina regularia*) from the late Smithian of Jiarong; F., Articulated bivalve clast with drusy spar internal fill; G., Articulated bivalve clast infilled with coarse spar and with an external coating of calcite crystals showing a fan-like morphology (white arrows), suggesting sea-floor precipitation; H., Pelsparite consisting of 70-80% peloids with crinoids, ostracodes and foraminifers and two intraclasts (blue arrows) composed of calcisphere wackestone. Some peloids show isopachous rim cements (green arrows) but most do not; I., Irregular coated grain, interpreted to be a pisoid (blue arrows), some degree of compaction is seen, Mingtang; J., Composite ooid with a thin oolitic coating; internal components include an ooid and two recrystallised grains with micritic envelopes, Mingtang; K., Ooid truncated by a stylolite showing later stage calcite cement overgrowth (blue arrows), *Ds. discreta* Zone of Jiarong.

Fig. 7. Pyrite framboid size-frequency distributions from Jiarong and Mingtang according to facies type. The dividing line between the dysoxic, anoxic and euxinic fields is based on experimental studies of Wilkin et al. (1996) and subsequently recalibrated and modified by Bond and Wignall (2010).

Fig. 8. SEM-BSE imagining and ^{57}Fe Mössbauer spectroscopy results. A., The bulk mineral composition of the Griotte Unit is mainly calcite and dolomite; B. and C., Non-carbonate minerals in the Griotte Unit; D., A (reworked?) pyrite framboid pseudomorph of ~6 μm size, EDX examinations (insets) show all sulfur has been replaced by oxygen; note the Si, Ca, Al signals are probably from surrounding carbonates; E., Elemental mapping shows nanometer-scale iron oxides (green dots) dispersed in the Griotte facies; F., ^{57}Fe Mössbauer results show hematite is the main iron-bearing phase in red beds, comprising ~43% of all iron species. Other phases include Ti-Fe oxides, carbonates, silicates and possibly sulphides; No pyrite has been found in SEM-EDS examinations of the same sample (2 cm*2cm). Mineral abbreviations: Ap., apatite; Cal., calcite; Dol., dolomite; Hem., hematite; Ilm.,

ilmenite; Py., pyrite; Qtz., quartz; Rt., rutile; Zrn., zircon.

Fig. 9. SEM images of Mingtang conodonts. **1., 2., 7., 11., *Triassospathodus homeri*** (Bender, 1970), 1., MTC-39_i022, 2., MTC-39_i023, 7., MTC-39_i03, 11., MTC-02_i134; **3., 6., *Neospathodus sp.***, 3., 6., MTC-39_i02; **4., 14., *Ns. pusillus*** Orchard, 1995, 4., MTC 39_i024, 14., MTC 39_i016; **5., *Ns. brochus*** Orchard, 1995, MTC-39_i005; **8., *Ns. radialis*** Zhao and Orchard, 2008, MTC-11.5_i137; **9., *Tr. symmetricus*** Orchard, 1995, MTC-02_i133; **10., *Ns. curtatus*** Orchard, 1995, MTC-02_i132; **12. *Novispathodus abruptus*** Orchard, 1995, MTC-39_i029; 13., *Ns.* aff. *abruptus,* MTC-02_i129; **15., *Nv. triangularis*** (Bender, 1970), MTC 39_i026; **16., *Cratognathodus* sp.**, MTC 39_i028.

Fig. 10. Comparison of $\delta^{13}C$ across studied sections. The South China record is from Sun et al. (2012). Changh., Changhsingian; Gries., Griesbachian; Dien., Dienerian; Aeg., Aegean; Bith., Bithynian. Conodont zonations: 1., *Ds. discrete*; 2., *Parach.-Pachy.*; 3., *Nv., pingdingshanensis*; 4., *Ic. collinsoni*; 5., *Tr. homeri*; 6., *Tr. symmetricus*; 7., *Nv. triangularis.*

Figure 11. Comparison of carbon cycling (simplified) in modern open oceans and Early Triassic isolated platforms assuming a "high productivity" scenario. Highest organic carbon remineralization occurs in modern open oceans just below the euphotic zone (e.g., highly productive equatorial Pacific, Feely et al., 2004). In contrast, on Early Triassic isolated platforms, organic carbon remineralization mostly occurred in surface waters and at the water/sediment interface; remineralization below storm wave base was probably minor due to wide-spread anoxic/euxinic conditions. In comparable modern settings, inner platform δ^{13}Ccarb can be up to 4 ‰ lighter than open water $\delta^{13}C_{carb}$ (e.g., Patterson and Walter, 1994). CCD - carbonate compensation depth; DIC -dissolved inorganic carbon; TOC - total organic carbon. ▲ - ^{13}C enriched; ▼- ^{13}C depleted. Models are horizontally and vertically not to scale.

Table 1. Pyrite framboid size-frequency distributions from Mingtang and Jiarong. n = number of framboids counted per sample; FD = framboid diameter (μm); SD = standard deviation. Note that JR43 was not plotted on the Mean versus Standard Deviation plot (Fig. 7) due to its low framboid count.

Table 2. XRF data of major element variations in the Griotte Limestone and normal grey limestone. LOI, loss on ignition.

Table 3. Foraminifera recorded in the Mingtang and Jiarong sections.

References:

Allen, A.P., Brown, J.H., Gillooly, J.F. 2002. Global biodiversity, biochemical kinetics, and the energetic-equivalence rule. Science 297, 1545-1548.

Angiolini, L., Checconi, A., Gaetani, M., Rettori, R. 2010. The latest Permian mass extinction in the Alborz Mountains (North Iran). Geological Journal 45, 216-229.

Bond, D.P.G., Wignall, P.B., Racki, G. 2004. Extent and duration of marine anoxia during the Frasnian-Famennian (Late Devonian) mass extinction in Poland, Germany, Austria and France. Geological Magazine 141, 173-193.

Bond, D.P.G., Wignall, P.B. 2010. Pyrite framboid study of marine Permo-Triassic boundary sections: a complex anoxic event and its relationship to contemporaneous mass extinction. Bulletin of the Geological Society of America 122, 1265-1279.

Boyer, F., 1964. Observations stratigraphiques et structurales sur le Dévonien de la région de Caunes-Minervois (Feuille Carcassonne au 80.000 e). Bull. Serv. Carte Géol. France 60, 105-121.

Burns, R.G., 1994. Mineral Mössbauer spectroscopy: correlations between chemical shift and quadrupole splitting parameters. Hyper Interact 91:739–745

Chen, J., 2004. Macroevolution of Bivalvia after the End-Permian Mass Extinction in South China, in: Rong, J., Fang, Z. (Eds.), Mass Extinction and Recovery: Evidences from the Palaeozoic and Triassic of South China. University of Science and Technology of China Press, Heifei, pp. 647-700.

Chen, Y.L., 2011. Conodont biostratigraphy of the Lower Triassic at Jiarong section, Triassic at Upper Guandao section in South of Guizhou Province. MSc thesis, Faculty of Earth Science. China University of Geosciences (Wuhan), Wuhan, p. 67.

Chen, Y.L., Twitchett, R.J., Jiang, H.S., Richoz, S., Lai, X.L., Yan, C.B., Sun, Y.D., Liu, X.D., Wang, L.N., 2013. Size variation of conodonts during the Smithian–Spathian (Early Triassic) global warming event. Geology 41, 823-826.

Chen, Z.-Q., Tong, J.N., Fraiser, M.L., 2011. Trace fossil evidence for restoration of marine ecosystems following the end-Permian mass extinction in the Lower Yangtze region, South China. Palaeogeography, Palaeoclimatology, Palaeoecology 299, 449-474.

Cheung, W.W.L., Sarmiento, J.L., Dunne, J., Frölicher, T.L., Lam, V.W.Y., Deng Palomares, M.L., Watson, R., Pauly, D., 2013. Shrinking of fishes exacerbates impacts of global ocean changes on marine ecosystems. Nature Climate Change 3, DOI:10.1038/NCLIMATE1691.

Cózar, P., Vachard, D., Somerville, I.D., Berkhli, M., Medina-Varea, P., Rodríguez, S., Said, I. 2008. Late Viséan-Serpukhovian foraminiferans and calcareous algae from the Adarouch region (central Morocco), North Africa. Geological Journal 43, 463-485.

Enkin, R.J., Yang, Z., Chen, Y., Courtillot, V., 1992. Paleomagnetic constraints on the geodynamic history of the major blocks of China from the Permian to the present. Journal of Geophysical Research 97, 13953-13989.

Feely, R.A., Sabine, C.L., Schlitzer, R., Bullister, J.L., Mecking, S. and Greeley, D., 2004. Oxygen Utilization and Organic Carbon Remineralization in the Upper Water Column of the Pacific Ocean. Journal of Oceanography, 60: 45-52.

Fröbisch, J., Angielczyk, K.D., Sidor, C.A., 2010. The Triassic dicynodont *Kombuisia* (Synapsida, Anomodontia) from Antarctica, a refuge from the terrestrial Permian-Triassic mass extinction. Naturwissenschaften 97, 187-196.

Galfetti, T., Hochuli, P.A., Brayard, A., Bucher, H., Weissert, H., Vigran, J.O., 2007. Smithian-Spathian boundary event: Evidence for global climatic change in the wake of the end-Permian biotic crisis. Geology 35, 291-294.

Galfetti, T., Bucher, H., Martini, R., Hochuli, P.A., Weissert, H., Crasquin-Soleau, S., Brayard, A., Goudemand, N., Brühwiler, T., Kuang, G., 2008. Evolution of Early Triassic outer platform paleoenvironments in the Nanpanjiang Basin (South China) and their significance for the biotic recovery. Sedimentary Geology 204, 36-60.

Garzanti, E., Nicora, A., Rettori, R., 1998. Permo-Triassic boundary and Lower to Middle Triassic in South Tibet. Journal of Asian Earth Sciences 16, 143-157.

Gorski, C.A., Scherer, M.M., 2010. Determination of nanoparticulate magnetite stoichiometry by Mössbauer spectroscopy, acidic dissolution, and powder X-ray diffraction: a critical review. American Mineralogist 95, 1017 – 1026.

Grasby, S.E., Beauchamp, B., Embry, A., Sanei, H., 2012. Recurrent Early Triassic ocean anoxia. Geology 41, 175-178.

Haughton, P., Davis, C., McCaffrey, W., Barker, S. 2009. Hybrid sediment gravity flow deposits – classification, origin and significance. Marine and Petroleum Geology 26, 1900-1918.

Hallam, A., Wignall, P.B., 1997. Mass Extinctions and Their Aftermath. Oxford Univ. Press, Oxford, p. 320.

Higgins, J.A., Fischer, W.W. and Schrag, D.P., 2009. Oxygenation of the ocean and sediments: Consequences for the seafloor carbonate factory. Earth and Planetary Science Letters, 284(1–2): 25-33.

Horacek, M., Richoz, S., Brandner, R., Krystyn, L., Spötl, C., 2007. Evidence for recurrent changes in Lower Triassic oceanic circulation of the Tethys: The $\delta^{13}C$ record from marine sections in Iran. Palaeogeography, Palaeoclimatology, Palaeoecology 252, 355-369.

Irmis, R.B., Whiteside, J.H., 2012. Delayed recovery of non-marine tetrapods after the end-Permian mass extinction tracks global carbon cycle. Proceedings of the Royal Society B: Biological Sciences 279, 1310-1318.

Joachimski, M.M., Buggisch, W., 1993. Anoxic events in the late Frasnian – causes of the Frasnian-Famennian faunal crisis? Geology 21, 675-678.

Joachimski, M.M., 1997. Comparison of organic and inorganic carbon isotope patterns across the Frasnian-Famennian boundary. Palaeogeography, Palaeoclimatology, Palaeoecology 132, 133-145.

Kaim, A., Nützel, A., 2011. Dead bellerophontids walking — The short Mesozoic history of the Bellerophontoidea (Gastropoda). Palaeogeography, Palaeoclimatology, Palaeoecology 308, 190-199.

Komatsu, T., Naruse, H., Shigeta, Y., Takashima, R., Maekawa, T., Dang, H.T., Dinh, T.C., Nguyen, P.D., Nguyen, H.H., Tanaka, G., Sone, M., 2014. Lower Triassic mixed carbonate and siliciclastic setting with Smithian–Spathian anoxic to dysoxic facies, An Chau basin, northeastern Vietnam. Sedimentary Geology 300, 28-48.

Lehrmann, D.J., Wei, J., Enos, P., 1998. Controls on facies architecture of a large Triassic carbonate platform; the Great Bank of Guizhou, Nanpanjiang Basin, South China. Journal of Sedimentary Research 68, 311-326.

Lehrmann, D.J., Payne, J.L., Felix, S.V., Dillett, P.M., Wang, H., Yu, Y.Y., Wei, J.Y., 2003. Permian-Triassic Boundary Sections from Shallow-Marine Carbonate Platforms of the Nanpanjiang Basin, South China: Implications for Oceanic Conditions Associated with the End-Permian Extinction and Its Aftermath. Palaios 18, 138-152.

Li, S.Y., Tong, J.N., Liu K.Y., Wang, F.J. & Huo, Y.Y. 2007. The Lower Triassic cyclic deposition in Chaohu, Anhui Province, China. Palaeogeography Palaeoclimatology Palaeoecology 252, 188-199.

Meyer, K.M., Yu, M., Jost, A.B., Kelley, B.M., Payne, J.L., 2011. $\delta^{13}C$ evidence that high primary productivity delayed recovery from end-Permian mass extinction. Earth and Planetary Science Letters 302, 378-384.

Muttoni, G., Gaetani, M., Kent, D.V., Sciunnach, D., Angiolini, L., Berra, F., Garzanti, E., Mattei, M., Zanchi, A., 2009. Opening of the Neo-Tethys Ocean and the Pangea B to Pangea A transformation during the Permian. Geoarabia 14, 17-48.

Nestell, G.P., Kolar-Jurkovšek, T., Jurkovšek, B., Aljinovič, D. 2011. Foraminifera from the Permian-Triassic transition in western Slovenia. Micropaleontology 57, 197-222.

O'Dogherty, L., De Wever, P., Goričan, Š., Carter, E.S., Dumitrica, P., 2011. Stratigraphic ranges of Mesozoic radiolarian families. Palaeoworld 20, 102-115.

Orchard, M.J., 2007. Conodont diversity and evolution through the latest Permian and Early Triassic upheavals. Palaeogeography, Palaeoclimatology, Palaeoecology 252, 93-117.

Orchard, M.J., Zonneveld, J.P., 2009. The Lower Triassic Sulphur Mountain Formation in the Wapiti Lake area: lithostratigraphy, conodont biostratigraphy, and a new biozonation for the lower Olenekian (Smithian). Canadian Journal of Earth Sciences 46, 757-790.

Patterson, W.P., Walter, L.M., 1994. Depletion of ^{13}C in seawater ΣCO_2, on modern carbonate platforms: Significance for the carbon isotopic record of carbonates. Geology 22, 885-888.

Paull, R.K., 1983. Definition and stratigraphic significance of the Lower Triassic (Smithian) conodont *Gladigondolella meeki* n. sp. in the western United States. Journal of Paleontology 57, 188-192.

Payne, J.L., Lehrmann, D.J., Wei, J.Y., Orchard, M.J., Schrag, D.P., Knoll, A.H., 2004. Large Perturbations of the Carbon Cycle During Recovery from the End-Permian Extinction. Science 305, 506-509.

Peck, L.S., Clark, M.S., Morley, S.A., Massey, A., Rossetti, H. 2009. Animal temperature limits and ecological relevance: effects of size, activity and rates of change. Functional Ecology 23, 248-256.

Pörtner, H.O. 2010. Oxygen- and capacity-limitation of thermal tolerance: a matrix for integrating climate-related stressor effects in marine ecosystems. The Journal of Experimental Biology 213, 881-893.

Pörtner, H.O., Knust, R. 2007. Climate change affects marine fishes through the oxygen limitation of thermal tolerance. *Science* **315**, 95-97.

Préat, A., Mamet, B., Bernard, A., Gillan, D., 1999. Bacterial mediation, red matrices diagenesis, Devonian, Montagne Noire (southern France). Sedimentary Geology 126, 223–242.

Préat, A., Mamet, B., Stefano, P.D., Martire, L., Kolo, K., 2011. Microbially-induced Fe and Mn oxides in condensed pelagic sediments (Middle-Upper Jurassic, Western Sicily). Sedimentary Geology 237, 179-188.

Pruss, S.B., Corsetti, F.A., Bottjer, D.J., 2005. The unusual sedimentary rock record of the Early Triassic: A case study from the southwestern United States. Palaeogeography, Palaeoclimatology, Palaeoecology 222, 33-52.

Raiswell, R., Canfield, D., 2012. The Iron Biogeochemical Cycle Past and Present. Geochemical Perspectives 1, 1-215.

Saito, R. , Kaiho, K., Oba, M., Takahashi, S., Chen, Z.Q., Tong, J.N., 2013. A terrestrial vegetation turnover in the middle of the Early Triassic. Global and Planetary Change 105, 152-159.

Sharp, C.E., Brady, A.L., Sharp, G.H., Grasby, S.E., Stott, M.B., Dunfield, P.F., 2014. Humboldt's spa: microbial diversity is controlled by temperature in geothermal environments. ISME Journal 8, 1166-1174.

Shigeta, Y., Zakharov, Y.D., Maeda, H., Popov, A.M., 2009. The Lower Triassic System in the Abrek Bay Area, South Primorye, Russia. National Museum of Nature and Science, Tokyo, p. 218.

Solien, M.A., 1979. Conodont Biostratigraphy of the Lower Triassic Thaynes Formation, Utah. Journal of Paleontology 53, 276-306.

Song, H.J., Wignall, P.B., Chu, D.L., Tong, J.N., Sun, Y.D., Song, H.Y., He, W.H., Li, T. 2014. Anoxia/high temperature double whammy during the Permian-Triassic marine crisis and its aftermath. Scientific Reports 4:4132, DOI: 10.1038/srep04132.

Sepkoski, J.J., Bambach, R.K. and Droser, M.L., 1991. Secular changes in Phanerozoic event bedding and the biological overprint. In: G. Einsele, W. Ricken and A. Seilacher (Editors), Cycles and Events in Stratigraphy. Springer-Verlag, Berlin Heidelberg, pp. 298-312.

Stanley, S.M., 2009. Evidence from ammonoids and conodonts for multiple Early Triassic mass extinctions. Proceedings of the National Academy of Sciences of the United States of America 106, 15264–15267.

Sun, Y.D., Joachimski, M.M., Wignall, P.B., Yan, C.B, Chen, Y.L., Jiang, H.S., Wang, L.N., Lai, X.L., 2012. Lethally Hot Temperatures During the Early Triassic Greenhouse. Science 338, 366-370.

Sweet, W.C., Mosher, L.C., Clark, D.L., Collinson, J.W., Hasenmueller, W.A., 1971. Conodont Biostratigraphy of the Triassic, in: Sweet, W.C., Bergstrom, S.M. (Eds.), Symposium on Conodont Biostratigraphy. Geoloical Society of America Memoir, pp. 441-465.

Takahashi, S., Oba, M., Kaiho, K., Yamakita, S., Sakata, S., 2009. Panthalassic oceanic anoxia at the end of the Early Triassic: A cause of delay in the recovery of life after the end-Permian mass extinction. Palaeogeography, Palaeoclimatology, Palaeoecology 274, 185-195.

Wang, C.S., Hu, X.M., Huang, Y.J., Wagreich, M., Scott, R., Hay, W., 2011. Cretaceous oceanic red beds as possible consequence of oceanic anoxic events. Sedimentary Geology 235, 27-37.

Wang, H.M., Xingli, W., Rongxi, L., Wei, J.Y., 2005. Triassic Conodont Succession and Stage Subdivision of the Guandao Section, Bianyang, Luodian, Guizhou. Acta Palaeontologica Sinica 44, 611-642.

Wignall, P.B., Twitchett, R.J., 1999. Unusual intraclastic limestones in Lower Triassic carbonates and their bearing on the aftermath of the end-Permian mass extinction. Sedimentology 46, 303-316.

Wignall, P.B., Bond, D.P.G., Kuwahara, K., Kakuwa, Y., Newton, R.J., Poulton, S.W., 2010. An 80 million year oceanic redox history from Permian to Jurassic pelagic sediments of the Mino-Tamba terrane, SW Japan, and the origin of four mass extinctions. Global and Planetary Change 71, 109-123.

Wilkin, R.T., Barnes, H.L., Brantley, S.L., 1996. The size distribution of framboidal pyrite in modern sediments: An indicator of redox conditions. Geochimica et Cosmochimica Acta 60, 3897-3912.

Woods, A.D., Bottjer, D.J., Corsetti, F.A., 2007. Calcium carbonate seafloor precipitates from the outer shelf to slope facies of the Lower Triassic (Smithian-Spathian) Union Wash Formation, California, USA: Sedimentology and palaeobiologic significance. Palaeogeography, Palaeoclimatology, Palaeoecology 252, 281-290.

Woods, A.D., 2014. Assessing Early Triassic paleoceanographic conditions via unusual sedimentary fabrics and features. Earth-Science Reviews, 137(0): 6-18.

Yin, H., Yang, F., Huang, Q., Yang, H., Lai, X., 1992. The Triassic of Qinling Mountains. China University of Geosciences Press, Wuhan, p. 211.

Youngquist, W.L., 1952. Triassic conodonts from southeastern Idaho. Journal of Paleontology, 26(4): 650-655.

Ziegler, A.M., McKerrow, W.S. 1975. Silurian marine red beds. American Journal of Science 275, 31-56.

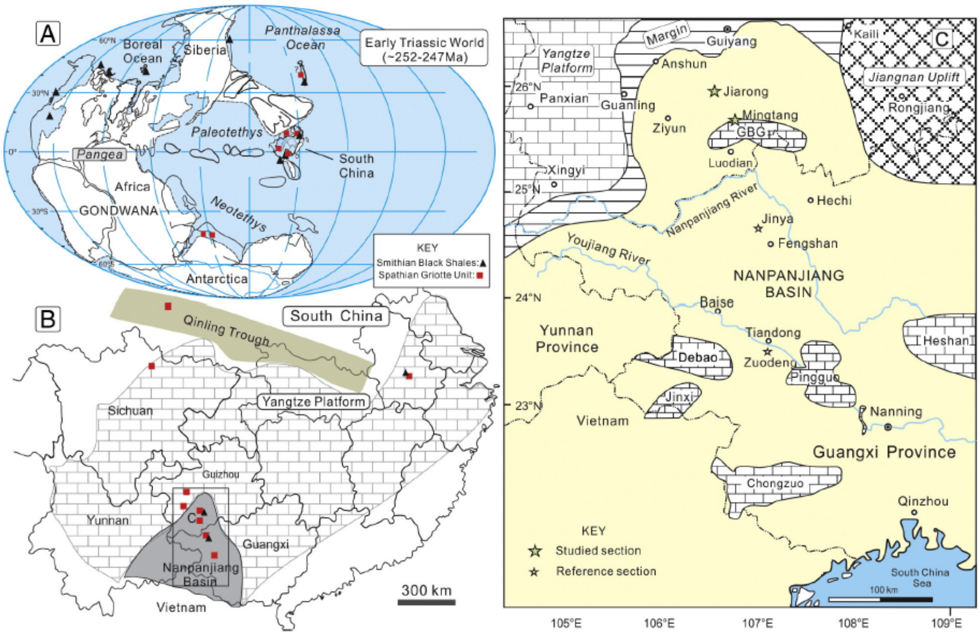

Fig. 1. A. Early Triassic palaeogeographic reconstructions of Pangea and Panthalassa, modified from Muttoni et al. (2009). The Spathian Griotte facies are widely distributed but are not known from the Boreal Ocean (Yin et al., 1992; Garzanti et al., 1998; Takahashi et al., 2009; Li et al., 2007 and this study). B. Relative positions of the Yangtze Platform, Nanapanjiang Basin and Qinling Trough. C. Palaeogeographic reconstruction of the Nanpanjiang Basin, after Lehrmann et al. (2003).

Figure 1 (above)

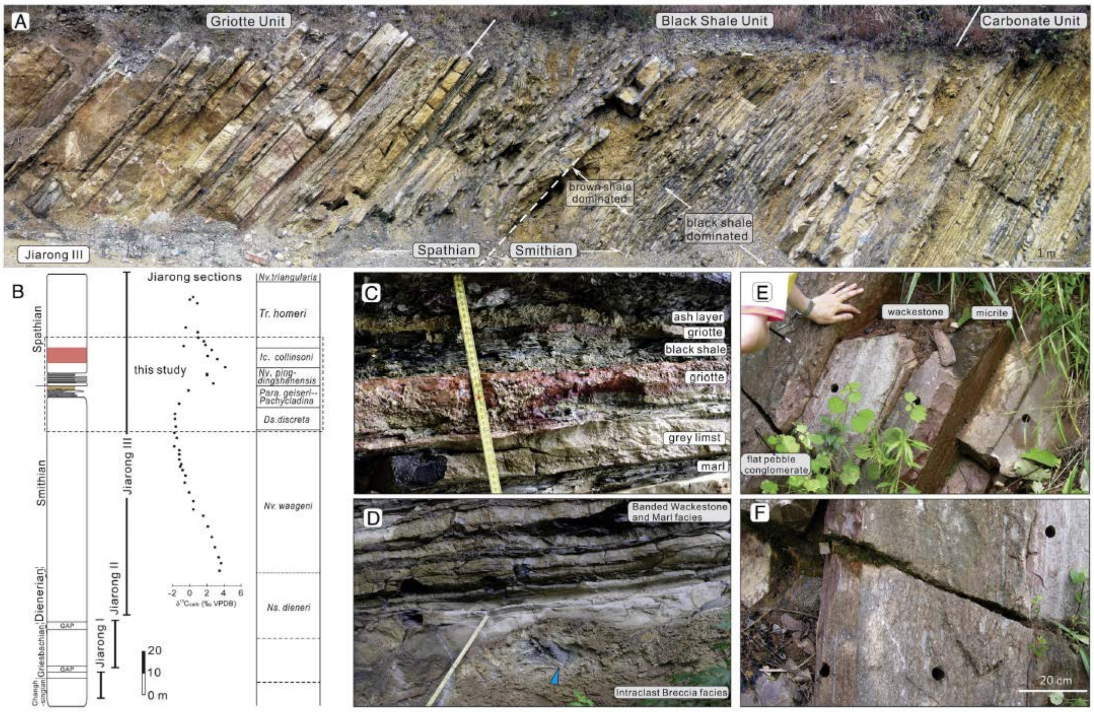

Fig. 2. Field photos of studied sections and biostratigraphic summary of Jiarong area. A. Field photograph of the middle and upper part of the Jiarong III section, showing three distinctive lithological units across the S-S boundary interval. B. Summary of the stratigraphic succession, conodont zones and the carbon isotope record of the Jiarong area. Conodont zonation is from Chen et al. (2013), carbon isotope data are from Sun et al. (2012). C. The lowermost part of the Griotte Unit at Jiarong III. Ruler is 35 cm in length. D. Intraclast breccia facies overlain by thin-bedded Banded Wackestone and Marl facies at Jiarong III. The blue arrow points to large, black shale clast. Ruler is 40 cm in length. E. The Griotte Unit at Mingtang showing red-colored wackestones, micrites and a flat pebble conglomerate bed. F. Flat pebble conglomerate bed in the lower Griotte Unit, Mingtang; pebbles range from less than 1 cm to 30 cm in size. Conodont abbreviations: *Ic.* = *Icriospathodus*; *Nv.* = *Novispathodus*; *Parach.* = *Parachirognathus*; *Tr.* = *Triassospathodus*.

Figure 2 (above)

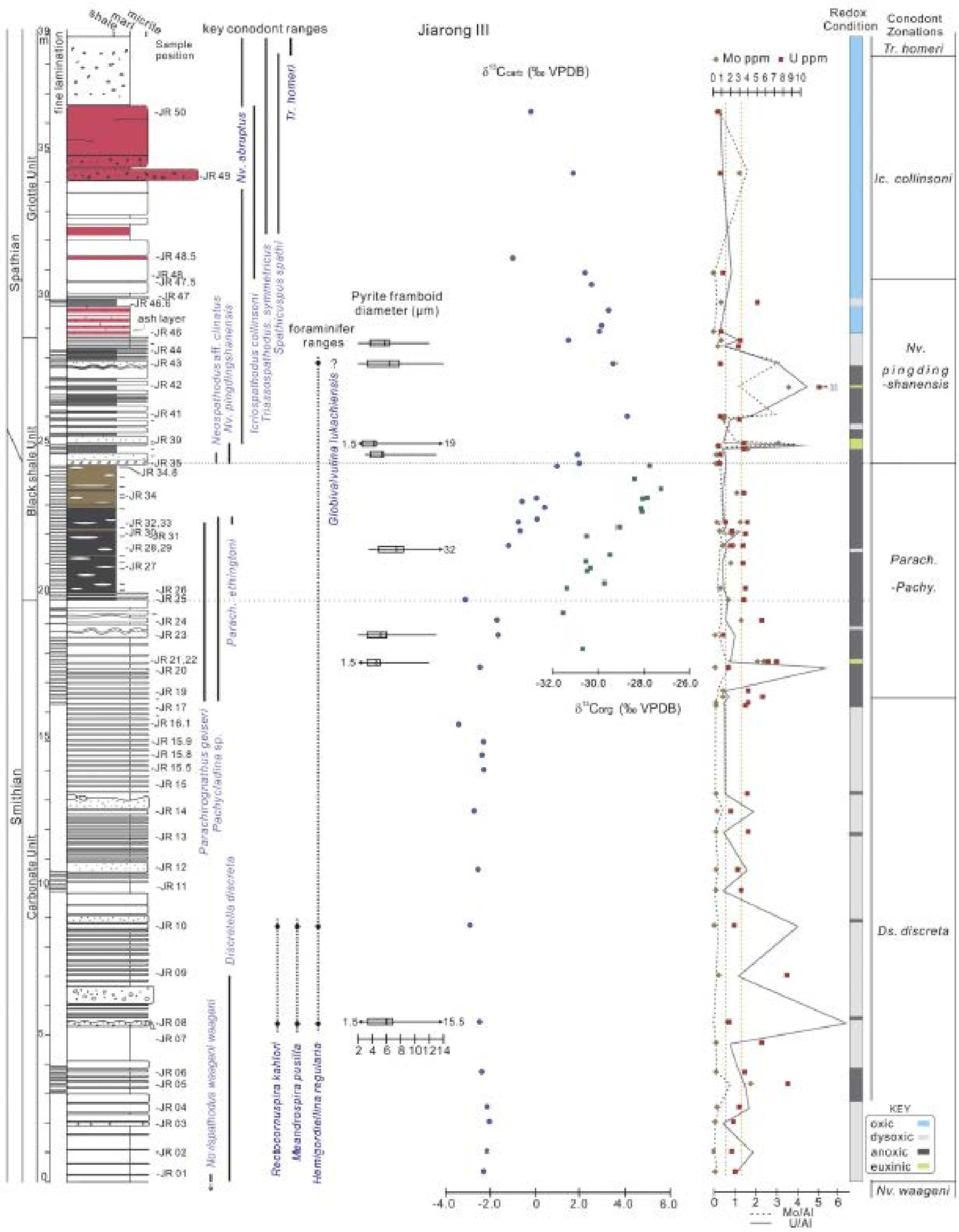

1050

1051 Figure 3 (above)

1052

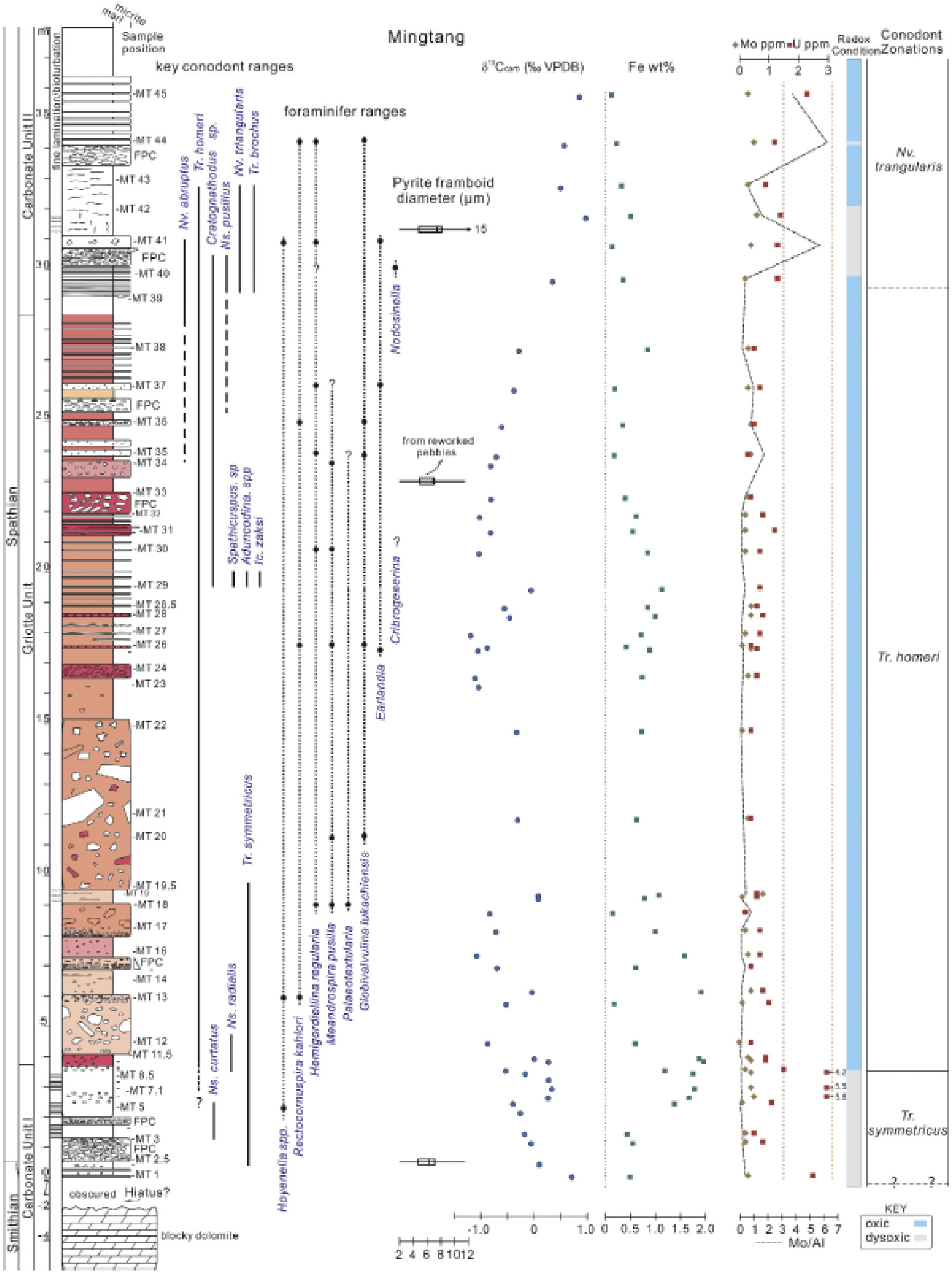

Figure 4 (above)

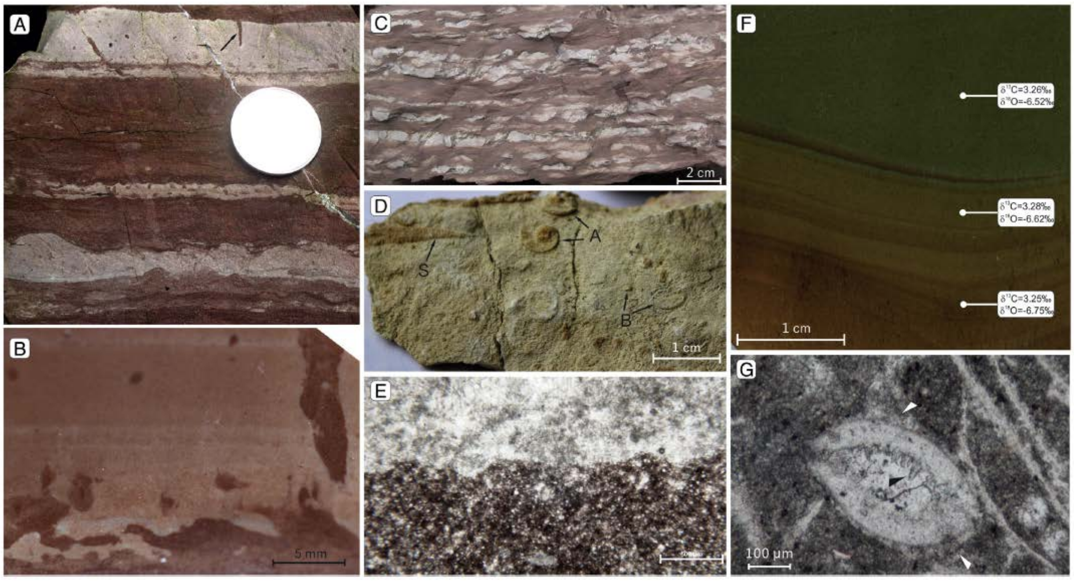

Fig. 5. Features of the Griotte Unit. A. Hand specimen showing small vertical and horizontal burrows (arrows), the coin is 1.5 cm in diameter. B. Polished slab of Griotte limestone (MT 19), showing both vertical "micro-*Skolithos*" and horizontal "micro-*Planolites*". C. Banded (alternating) wackestone and marl facies, beds become discontinuous and nodular in appearance. D. Hand specimen of Griotte limestone, showing early Spathian bioclasts [consisting of unusually small ammonoids (A), bivalves (B) and scaphopods (S)] developed in the aftermath of the S-S crisis. E. Thin section photo, showing the sharp, undulatory contact between griotte and gray limestone. F. Polished slab of the Griotte limestone showing the gray-greenish micrite in contact with red micrite. $\delta^{13}C_{carb}$, sampled with a small dental dill, shows no significant changes across the contact. G. A photomicrograph of the Griotte limestone shown in D, molluscan wackestone with cephalopod/bivalve shells, thick-shelled ostracodes, calcispheres and rare peloids. The ostracode shows both external encrustation (white arrow) and fringing bladed cements of variable thickness (black arrow).

Figure 5 (above)

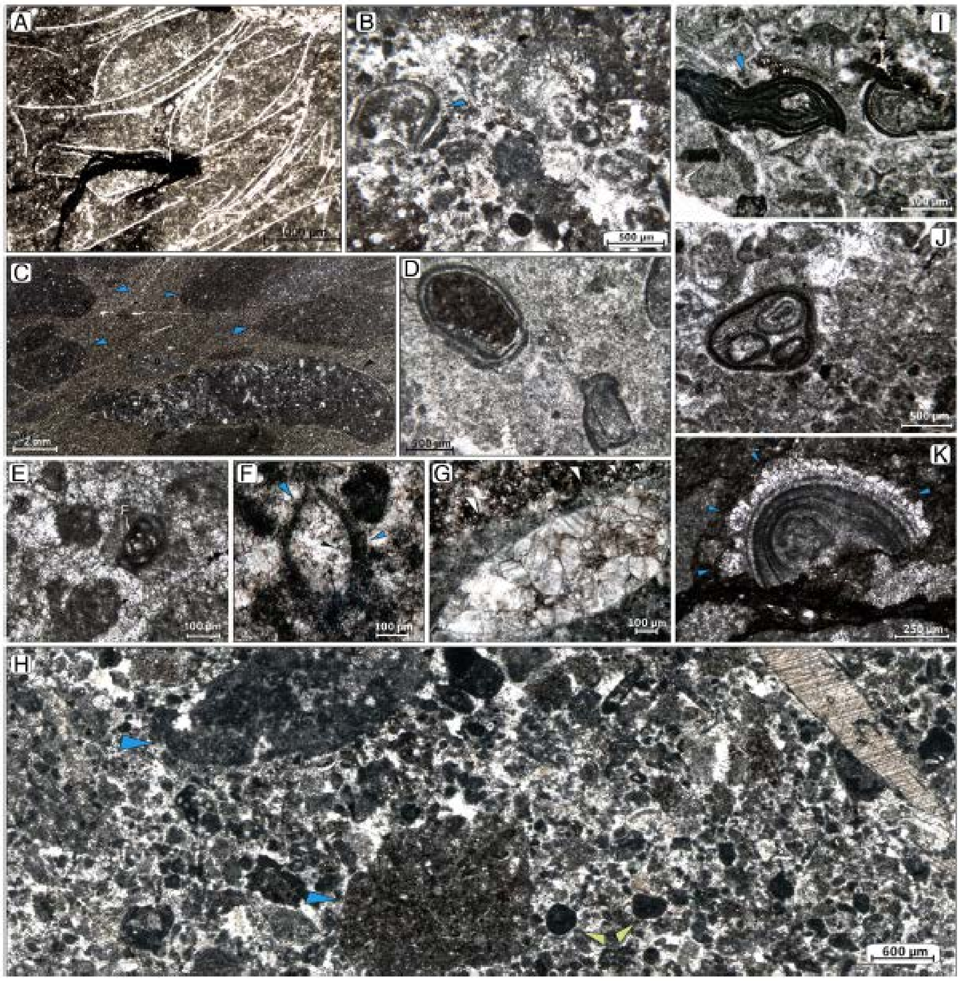

Fig. 6. Carbonate thin-section photographs of Jiarong and Mingtang sections. A. Filamentous wacke-packstones. B. Pelsparite with dark round peloids and thin bivalves shells. Note the thick micritic envelope that has developed on the shell (blue arrow). C. Flat pebble conglomerate (FPC) fabric from the Griotte Unit. Most pebbles are calcisphere wackestones except for one (black arrow) which is a peloidal packstone with thin-shelled bivalves, crinoids and foraminifers. D. Superficial ooid with a peloid nucleus. The peloids are darker and finer-grained than the matrix suggesting aggrading neomorphism of the latter. E. A small benthic foraminifer (*Hemigordiellina regularia*) from the late Smithian of Jiarong. F. Articulated bivalve clast with drusy spar internal fill. G. Articulated bivalve clast infilled with coarse spar and with an external coating of calcite crystals showing a fan-like morphology (white arrows), suggesting sea-floor precipitation. H. Pelsparite consisting of 70–80% peloids with crinoids, ostracodes and foraminifers and two intraclasts (blue arrows) composed of calcisphere wackestone. Some peloids show isopachous rim cements (green arrows) but most do not. I. Irregular coated grain, interpreted to be a pisoid (blue arrows), some degree of compaction is seen, Mingtang. J. Composite ooid with a thin oolitic coating; internal components include an ooid and two recrystallized grains with micritic envelopes, Mingtang. K. Ooid truncated by a stylolite showing later stage calcite cement overgrowth (blue arrows), *Discretella discreta* Zone of Jiarong.

Figure 6 (above)

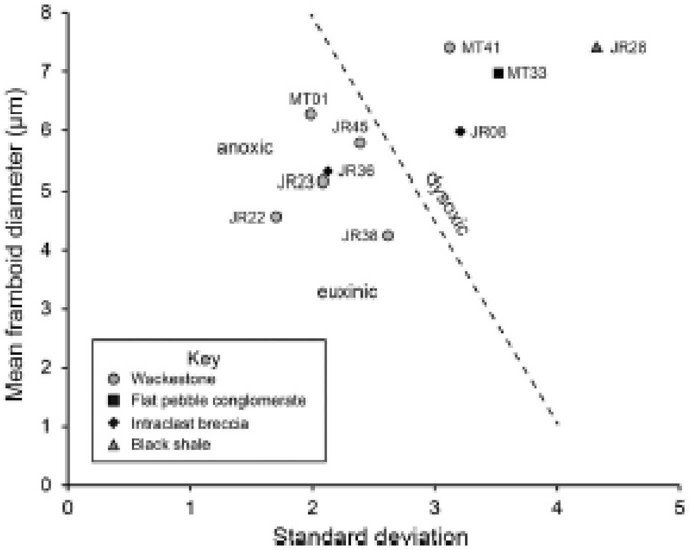

Fig. 7. Pyrite framboid size–frequency distributions from Jiarong and Mingtang according to facies type. The dividing line between the dysoxic, anoxic and euxinic fields is based on experimental studies of Wilkin et al. (1996) and subsequently recalibrated and modified by Bond and Wignall (2010).

Figure 7 (above)

Table 1
Pyrite framboid size–frequency distributions from Mingtang and Jiarong. n = number of framboids counted per sample; FD = framboid diameter (μm); SD = standard deviation. Note that JR43 was not plotted on the mean versus standard deviation plot (Fig. 7) due to its low framboid count.

Sample	Lithology	n	Mean FD	SD	Min FD	Max FD
MT01	Wackestone	101	6.27	1.99	2	11.5
MT33	Intraclast breccia	18	6.97	3.5	2	11.5
MT41	Wackestone	22	7.41	3.12	3.5	15
JR08	Intraclast breccia	68	5.98	3.2	1.5	15.5
JR22	Wackestone	56	4.56	1.7	1.5	12
JR23	Wackestone	79	5.15	2.08	2	13
JR28	Black shale	50	7.42	4.32	3.5	32
JR36	Flat pebble conglomerate	29	5.31	2.12	3	13
JR38	Wackestone	50	4.25	2.62	1.5	19
JR43	Flat pebble conglomerate	6	6.42	4.25	2	14
JR45	Wackestone	92	5.78	2.39	2	12

Table 1 (above)

Table 2
XRF data of major element variations in the Griotte Limestone and normal gray limestone. LOI, loss on ignition. Values are in wt %.

Sample	Lithology	SiO_2	TiO_2	Al_2O_3	Fe_2O_3	MnO	MgO	CaO	Na_2O	K_2O	P_2O_5	LOI	Summary %
MT08	gray marl	33.01	0.39	7.90	2.69	0.06	9.54	18.12	0.04	2.30	0.14	25.71	99.90
MT14R	red marl	24.28	0.30	6.19	2.63	0.03	7.31	27.82	0.14	1.81	0.13	29.28	99.91
MT19R	red limst	16.43	0.15	2.89	1.15	0.04	14.08	27.12	<0.01	0.87	0.13	37.07	99.93
MT24R	red limst	13.42	0.18	2.13	1.01	0.02	0.93	45.14	<0.01	0.59	0.10	36.34	99.94
MT35	gray limst	3.10	0.08	0.49	0.42	0.03	1.15	68.27	<0.01	0.24	0.06	26.10	99.95
MT40	gray limst	4.59	0.09	1.07	0.67	0.03	4.92	59.06	<0.01	0.37	0.10	29.04	99.93
MT42	gray limst	2.61	0.06	0.58	0.62	0.02	8.87	54.21	<0.01	0.22	0.36	32.41	99.94

Table 2 (above)

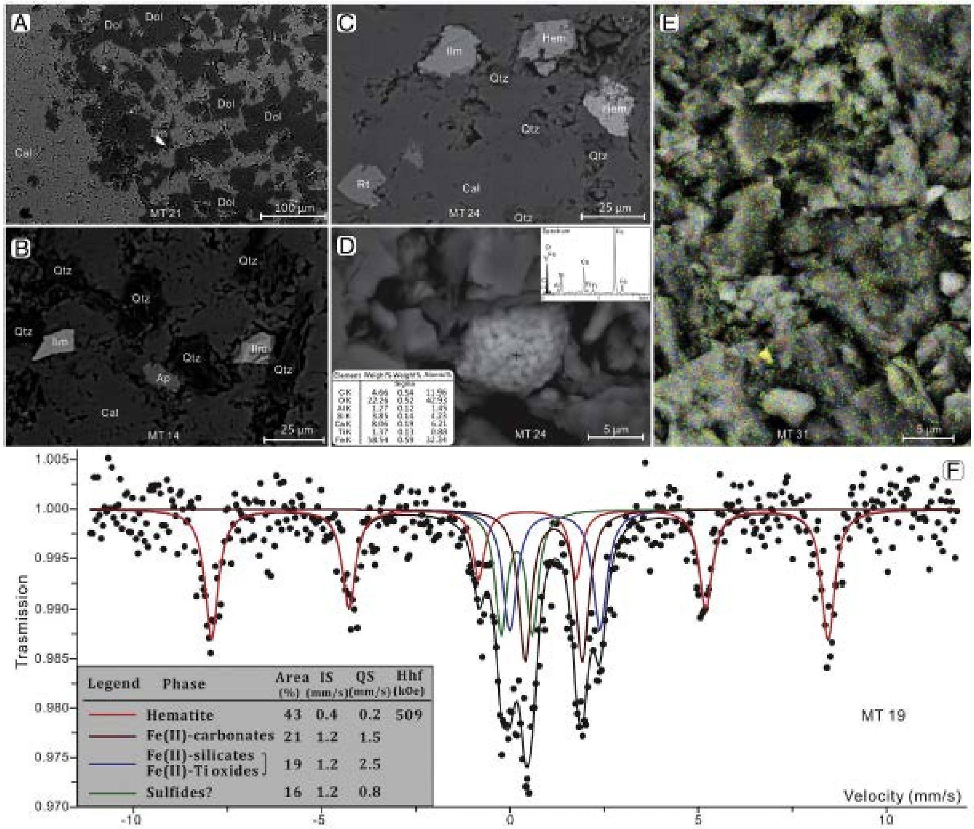

Fig. 8. SEM-BSE imagining and ^{57}Fe Mössbauer spectroscopy results. A. The bulk mineral composition of the Griotte Unit is mainly calcite and dolomite. B and C. Non-carbonate minerals in the Griotte Unit. D. A (reworked?) pyrite framboid pseudomorph of ~ 6μm size, EDX examinations (insets) show all sulfur has been replaced by oxygen; note the Si, Ca, Al signals are probably from surrounding carbonates. E. Elemental mapping shows nanometer-scale iron oxides (green dots) dispersed in the Griotte facies. F. ^{57}Fe Mössbauer results show hematite is the main iron-bearing phase in red beds, comprising ~43% of all iron species. Other phases include Ti–Fe oxides, carbonates, silicates and possibly sulfides. No pyrite has been found in SEM-EDS examinations of the same sample (2 cm * 2 cm). Mineral abbreviations: Ap., apatite; Cal., calcite; Dol., dolomite; Hem., hematite; Ilm., ilmenite; Py., pyrite; Qtz., quartz; Rt., rutile; Zrn., zircon.

Figure 8 (above)

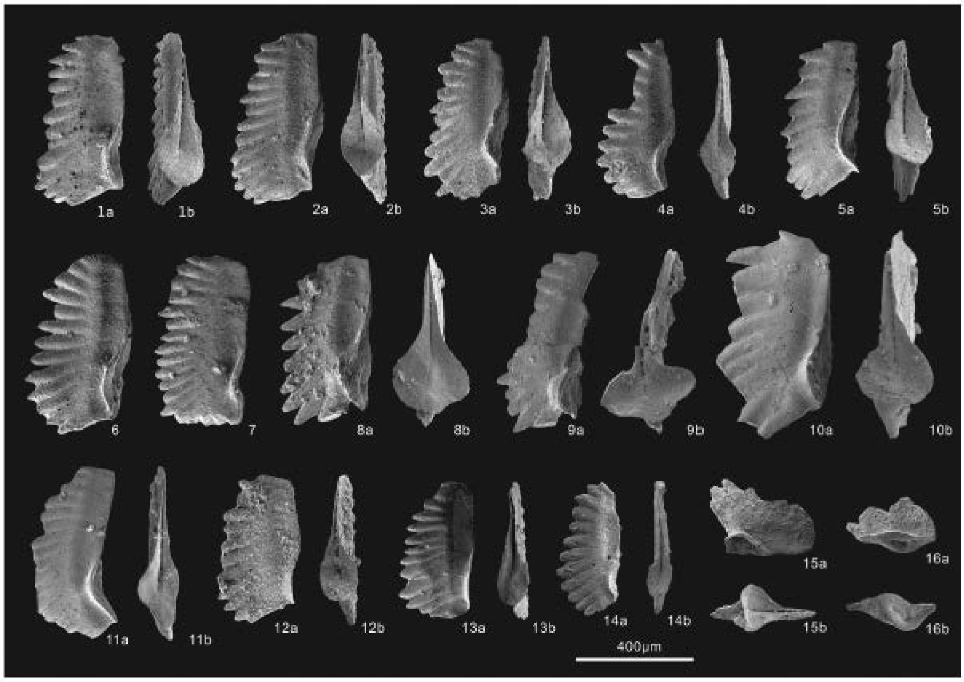

Fig. 9. SEM images of Mingtang conodonts. **1, 2, 7, 11,** ***Triassospathodus homeri*** (Bender, 1970), 1, MTC-39_i022, 2, MTC-39_i023, 7, MTC-39_i03, 11, MTC-02_i134; **3, 6,** ***Neospathodus*** **sp.**, 3, 6, MTC-39_i02, MTC-39_i024; **4, 14,** ***Neospathodus pusillus*** Orchard, 1995, 4, MTC 39_i024, 14, MTC 39_i016; **5,** ***Neospathodus brochus*** Orchard, 1995, MTC-39_i005; **8,** ***Neospathodus radialis*** Zhao and Orchard, 2008, MTC-115_i137; **9,** ***Triassospathodus symmetricus*** Orchard, 1995, MTC-02_i133; **10,** ***Neospathodus curtatus*** Orchard, 1995, MTC-02_i132; **12** ***Novispathodus abruptus*** Orchard, 1995, MTC-39_i029; 13, ***Neospathodus*** **aff.** ***abruptus***, MTC-02_i129; **15,** ***Novispathodus triangularis*** (Bender, 1970), MTC 39_i026; **16,** ***Cratognathodus*** **sp.**, MTC 39_i028.

Figure 9 (above)

Table 3
Foraminifera recorded in the Mingtang and Jiarong sections.

Sample	Taxa							
	Hoyenella spp.	*Rectocornuspira kahlori*	*Hemigordiellina regularia*	*Meandrospira pusilla*	*Palaeotextularia*	*Globivalvulina lukachiensis*	*Earlandia*	*Cribrogenerina*	*Nodosinella*
MT05	x								
MT13	x	x							
MT18			x	x	x				
MT20				x		x			
MT25							x		
MT26		x		x		x			
MT30			x	x				?	
MT34				x					
MT35			x		?	x			
MT36		x				x			
MT37			x	?			x		
MT40			?						x
MT41	x		x				x		
MT44		x	x			x			
JR8		x	x	x					
JR10		x	x	x					
JR43			x			?			

Table 3 (above)

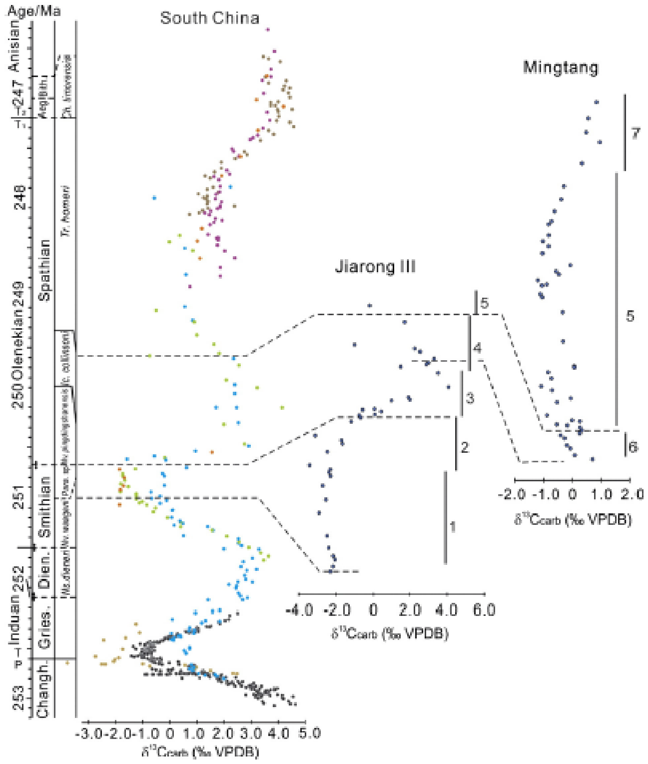

Fig. 10. Comparison of $\delta^{13}C$ across studied sections. The South China record is from Sun et al. (2012). Changh., Changhsingian; Gries., Griesbachian; Dien., Dienerian; Aeg., Aegean; Bith., Bithynian. Conodont zonations: 1, *Discretella discreta*; 2, *Parachirognathus–Pachycladina*; 3, *Novispathodus pinglingshanensis*; 4, *Icriospathodus collinsoni*; 5, *Triassospathodus homeri*; 6, *Triassospathodus symmetricus*; 7, *Novispathodus triangularis*.

Figure 10 (above)

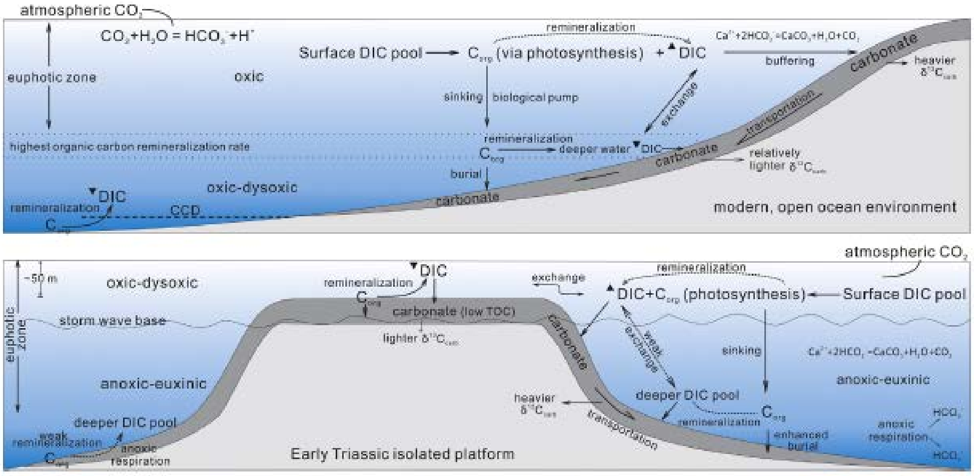

Fig. 11. Comparison of carbon cycling (simplified) in modern open oceans and Early Triassic isolated platforms assuming a "high productivity" scenario. Highest organic carbon remineralization occurs in modern open oceans just below the euphotic zone (e.g., highly productive equatorial Pacific, Feely et al., 2004). In contrast, on Early Triassic isolated platforms, organic carbon remineralization mostly occurred in surface waters and at the water/sediment interface; remineralization below storm wave base was probably minor due to wide-spread anoxic/euxinic conditions. In comparable modern settings, inner platform $\delta^{13}C_{carb}$ can be up to 4 ‰ lighter than open water $\delta^{13}C_{carb}$ (e.g., Patterson and Walter, 1994). CCD, carbonate compensation depth; DIC, dissolved inorganic carbon; TOC, total organic carbon. ▲, ^{13}C enriched; ▼, ^{13}C depleted. Models are horizontally and vertically not to scale.

Figure 11 (above)